Theoretical formulation of phase space microbunching instability in the presence of intrabeam scattering for single-pass or recirculation accelerators

Cheng-Ying Tsai,[1,2,*] Weilun Qin,[3,†] Kuanjun Fan,[4] Xiaofan Wang,[5] Juhao Wu,[2] and Guanqun Zhou[2]

[1]*Department of Electrotechnical Theory and Advanced Electromagnetic Technology, Huazhong University of Science and Technology, Wuhan, 430074, China*
[2]*SLAC National Accelerator Laboratory, Menlo Park, California 94025, USA*
[3]*Department of Physics, Lund University, PO Box 118, Lund 22100, Sweden*
[4]*State Key Laboratory of Advanced Electromagnetic Engineering and Technology, School of Electrical and Electronic Engineering, Huazhong University of Science and Technology, Wuhan, 430074, China*
[5]*Shanghai Institute of Applied Physics, Chinese Academy of Sciences, Shanghai 201800, China*

(Received 3 September 2020; accepted 1 December 2020; published 14 December 2020)

Microbunching instability (MBI) has been one of the most challenging issues in designs of high-brightness beam transport lines for single-pass or recirculating accelerators. Although the intrabeam scattering (IBS) has long been studied in lepton or hadron storage rings as a slow diffusion process or in high-intensity proton linear accelerators as one mechanism for the beam halo, the effects of IBS on single-pass or recirculating electron accelerators have drawn attention only in the recent two decades due to emergence of linac-based or energy-recovery-linac-based fourth-generation light sources, which require high-quality electron beams during the beam transport. In this paper we develop a theoretical formulation of microbunching instability in the presence of IBS for single-pass or recirculation accelerators. To quantify MBI with inclusion of IBS, we start from the Vlasov-Fokker-Planck (VFP) equation, combining both collective interactions and incoherent IBS effects. The linearized VFP equation and the corresponding friction and diffusion coefficients are derived. The evolutions of the resultant density and energy modulations are formulated as a set of coupled integral equations. The theoretical formulation is then applied to a recirculating beamline design. The results from the semianalytical calculation are compared and show good agreement with massive particle tracking simulations.

DOI: 10.1103/PhysRevAccelBeams.23.124401

I. INTRODUCTION

In the last two decades, microbunching instability (MBI) has been recognized as a challenging issue in high-brightness electron beam transport and intensive studies have been done in linear accelerators (linac) [1], storage-ring accelerators [2], and recirculating or energy-recovery-linac (ERL) accelerators [3]. For single-pass or few-passes key transport line designs with applications to, e.g., bunch compressor chicanes in the fourth-generation light sources [4] or electron cooling facilities in the next-generation electron-ion colliders [5,6], the typical normalized transverse beam emittance can be 1 μm or lower, the uncorrelated beam energy spread 10^{-4} or smaller. Such a high-brightness electron beam can be susceptible to the collective effects due to either the interaction between the beam and the environment or the beam itself, leading to beam quality degradation. For the latter, the relevant collective effects of our interest include the coherent synchrotron radiation (CSR) and the longitudinal space charge (LSC). When an electron beam traverses a series of bending magnets, CSR due to coherent radiation emission inside the bends can induce a correlated energy modulation along the bunch, and the subsequent nonzero longitudinal dispersion or momentum compaction R_{56} can have a significant effect on converting the energy modulation to the density modulations downstream the beamline [7–11]. LSC stems from upstream density ripples on top of the bunch charge density, and can generate an amount of energy modulation when the beam goes through a long straight section of a beamline [12–14]. In a linac or recirculating accelerator, a transport line is usually composed of a series of straight and intervening bending (dispersive) magnetic elements, meaning the consecutive density-energy conversions. Once such a density-energy conversion forming a positive feedback, it may lead to the enhancement of modulation amplitudes. This has been known as the MBI.

*jcytsai@hust.edu.cn
†weilun.qin@sljus.lu.se

Particularly, a recirculation arc with multiple (usually several to tens of) bending magnets can convert the upstream accumulated energy modulations into density modulations, resulting in deleterious phase space degradation. In this aspect, MBI is usually undesirable in high-brightness beam transport.

MBI, in another aspect, has however been recognized as an important and necessary scheme that makes short-wavelength high-intensity laser possible, e.g., VUV or x-ray free-electron laser (XFEL) (see, for example, Refs. [15–20] and references therein). Typical operating modes for short-wavelength FELs include SASE (self-amplification spontaneous emission) [16] and seeded modes. In the SASE mode, the amplification process originates from shot noise of the otherwise microbunched electron beam. Through the process of FEL collective instability, the electron beam will be microbunched/modulated at the resonant wavelength and the output characteristics of SASE FEL, upon saturation, will feature the full transverse coherence, though its temporal or spectral profile can be noisy [18–20]. The seeded mode operation, acting as an amplifier, indeed requires an input source. It has been known that utilizing higher harmonics generation, e.g., high-gain harmonics generation (HGHG) [17,21] or echo-enabled harmonic generation (EEHG) [22,23] can be an option. Another option is the so-called self-seeding [24–26]. In the self-seeding option the FEL system starts with the first section of undulators based on SASE mode and is followed by a crystal monochromator or gratings to purify the output spectrum, serving as the subsequent input signal. A second section of undulators proceeds and amplifies the purified signal until saturation. Compared with SASE, the output characteristics of a seeded FEL are with much narrower spectral bandwidth and better wavelength stability (see, for example, Refs. [18–20] for more details). Recent theoretical [27] and experimental [28,29] studies show that, when a microbunched (prebunched) electron beam enters an undulator, mixture of the modulation wavelength of the prebunched beam and the FEL resonant wavelength will lead to the so-called MBI-induced pedestal sideband instability in the exponential-growth (linear) regime. Here we should note that the physical mechanism is essentially different from the traditional FEL sideband instability [30–32], where the microbunched electron beam becomes trapped in the ponderomotive potential well and executes synchrotron motion in the post-saturation regime. Therefore, from this aspect, FEL has become an excellent example of positive reinforcement of MBI, except for fewer undesirable side effects.

In typical situations a high-brightness electron beam would go through the above two stages; undesirable is mostly the first stage. A compromised device, the laser heater [33–35], has been introduced to impose a small amount of energy spread (strictly speaking, energy modulation) to the electron beam in order to enhance phase space smearing (or Landau damping) to suppress the MBI before it potentially breaks up the high-brightness electron beam, while to retain the slice energy spread within the design goal before the electron beam enters the undulator. Nowadays the laser heating technique has been incorporated for almost all linac-based short-wavelength FEL projects. However, introduction of laser heaters in recirculating accelerators may not be practical, and in the meanwhile the induced trickle heating issues [35,36] downstream the beamline, sensitive to the beam optics, are needed to resolve. Therefore, a careful analysis of MBI is practical and essential to realize in depth both the high-brightness beam transport and the ultimate performance of MBI-driven FEL mechanism.

There have been intensive studies on MBI in single-pass or recirculating accelerators, in analytical or semi-analytical [7–9,13,14,37,38], numerical [10,11,39–41], and experimental [35,36,42] frameworks. This work extends the existing theoretical formulation [13] by including the effect of intrabeam scattering (IBS) in the semianalytical way, as will be exploited below. Since we do not directly solve the phase space distribution function using numerical mesh, the numerical noise issue will not be a limiting factor and the numerical computation will be much faster than the particle tracking simulation. This allows us to perform systematic studies or machine optimization more effectively.

In most situations, IBS has long been studied in lepton or hadron storage rings as a slow diffusion process (see, for example, Ref. [43] and references therein), in low-emittance damping rings for future linear colliders (see, for example, Ref. [44]), or in high-intensity proton linear accelerators as one mechanism for the beam halo (see, for example, Refs. [45,46]). The effects of IBS on single-pass or few-passes recirculating electron accelerators have drawn attention only in the recent two decades due to emergence of linac-based or ERL-based fourth-generation light sources, which require excellent high quality electron beams, not only from beam generation but also during the beam transport, i.e., less tolerance of beam quality degradation, for even smaller beam emittance, extremely low energy spread, and higher bunch charges. The IBS is the multiple small-angle Coulomb scattering of charged particles, involves the momentum transfer between the transverse and longitudinal directions, and is responsible for changes or rearrangement of distribution core, eventually leading to an equilibrium state, or diffusing slowly and growing indefinitely [47]. In contrast, Touschek scattering, which relates the single large-angle scattering and momentum transfer from the transverse to longitudinal direction, and is responsible for creation of distribution tails or particle loss [47]. Here we do not consider Touschek effect, because for the moment we are only interested in microbunching, which typically occurs in the core of the beam. It is known that the IBS is an accumulation effect, where the instantaneous growth rate is proportional to the

beam charge density or bunch current, and inversely proportional to the beam energy, transverse emittance and energy spread, i.e., $\tau_{\mathrm{IBS}}^{-1} \propto N/\gamma^2\epsilon_x^N\epsilon_y^N\sigma_z\sigma_\delta$, where N is the number of particles per bunch, γ the Lorentz relativistic factor, $\epsilon_{x,y}^N$ the normalized transverse emittance, σ_z the bunch length, and σ_δ the relative energy spread [see Eqs. (1)–(4) in Sec. II]. In a storage ring configuration, e.g., a damping ring, the beam energy ∼GeV, number of particles 10^{10} or more (corresponding to a peak bunch current 50–100 A), normalized transverse emittance ∼μm, and energy spread $\sim 10^{-4}$–10^{-3}, can be typical parameters [48]. In the middle or low-energy single-pass electron accelerators, typical parameters are: the beam energy ∼100 MeV, bunch population of $10^8 \sim 10^9$ (corresponding to a comparable or higher peak bunch current), normalized transverse horizontal emittance ∼μm or smaller, energy spread $\sim 10^{-5}$–10^{-4}. It can be seen that the IBS growth rate for the latter is two or three orders of magnitude larger than that of the former. If a beam with a proper energy chirp passes through a bunch compressor section, the local bunch current can have large enhancement, e.g., a factor of 10 to 100 enhancement, and the IBS effect may become more evident. Although the electron beam in a single-pass or recirculating accelerator may only travel at a distance of ∼100 m to ∼km, the aforementioned enhancement may lead to a small but visible effect on MBI. Therefore, an analysis of MBI in the presence of IBS shall have potential practical interest.

Some preliminary analytical estimate [48] and massive start-to-end particle tracking simulation (e.g., Ref. [49], though IBS is not included throughout the whole beamline) in the Linac Coherent Light Source (LCLS) were presented with inclusion of IBS, and the results from both do not expect the IBS to significantly affect FEL operation. However, a recent experiment performed at FERMI linac [50], together with an analytical estimate and preliminary particle tracking simulations, indicates that the contribution of IBS can be significant for operating configurations of VUV and soft x-ray FEL. Including the IBS effect into the overall performance evaluation would help realize accessible, practical potential performance.

Here we note that in Refs. [48,50,51] the analytical estimate only takes into account the longitudinal phase space smearing (or energy Landau damping) with IBS-induced slice energy spread increase, and the analysis is restricted to a simplified linac-drift transport, followed by a bunch compressor chicane (parametrized by the compression factor C and momentum compaction R_{56}). While the transverse phase space smearing due to the initial intrinsic beam emittance is considered following Ref. [8,9], to our knowledge such effect of beam emittance growth arising from IBS is not included in the existing microbunching analysis. As we will explore in this paper, the inclusion of both IBS-induced emittance growths and energy spread increase is necessary to obtain consistent and correct scaling relations. Moreover, the above mentioned analytical estimates ignore the dynamical friction and diffusion effects associated with IBS. Although the analysis gives the final microbunching gain, it does not reveal how the gain evolves along the beamline. This will limit the applicability to the recirculating accelerators, where the behavior of microbunching development in the multi-bend transport line can be complicated. The emphasis of Ref. [50] is put on the estimate of the slice energy spread, which plays an essential role in ultimate linac-driven FEL performance, and their comparison with experimental measurements. Overall, there is still lack of a dedicated theoretical formulation of microbunching instability for single-pass or recirculating accelerators to include the six-dimensional (6-D) beam dynamics with inclusion of collective effects and the incoherent IBS effect in a general beam transport line. This serves as a motivation of this work. Together with our developed theoretical formulation, we adopt an existing IBS model, based on the completely integrated modified Piwinski approximation (CIMP) [52]. Use of CIMP greatly reduces the computing time for many calculations involving IBS, while retains variation of lattice parameters in single-pass or recirculating beamlines. We apply our developed theoretical formulation to a recirculating beamline design. The results from the semianalytical calculation are compared and show good agreement with massive particle tracking simulations using ELEGANT [53,54].

Overall, the contributions of this work may be summarized as follows. First, the 6-D phase space microbunched dynamics is formulated based on the Vlasov-Fokker-Planck (VFP) framework. The corresponding friction and diffusion coefficients are derived following a similar procedure to Ref. [55]. The effect of IBS is attributed by the zeroth-order dynamics, assuming the (unperturbed) Gaussian phase space distribution, and also contributes to enhancement of the phase space smearing. The aforementioned collective effects and the IBS friction and diffusion effects are then connected with the first-order dynamics. The resultant linear coupled integral equations are expressed in terms of the density and energy modulations. Second, the developed semianalytical formulation is applied to a practical recirculating beamline. The results from the semi-analytical calculation are benchmarked, compared and show good agreement with massive particle tracking simulations using ELEGANT. We believe that the developed formulation shall be generally applicable for linear analysis of 6-D phase space dynamics for single-pass high-brightness beams in the presence of both collective and incoherent effects. Since the semianalytical calculation is much faster than the particle tracking simulations, together with the developed formulation, we hope that it may be applied to investigate the interplay among the beam collective effects, the incoherent scattering effects, and those dependences on lattice parameters with a linear transport line optics design in a systematic way.

In the remainder of this paper, the IBS formulas based on CIMP are briefly introduced in Sec. II. Since the detailed derivation of the full IBS theory is complicated and not of our focus, we only quote the main results and highlight the model assumptions behind this IBS model. In Sec. III we formulate the 6-D phase space dynamics of an electron beam with IBS based on the VFP framework. For simplicity, to include the Coulomb scattering, the VFP equation is first formulated in the beam rest frame (Sec. III A), and the friction and diffusion coefficients are derived (Sec. III B). Then the VFP equation is Lorentz transformed back to the lab frame to study the phase space dynamics in the presence of collective effects (Sec. III C). Since the onset of MBI is of our primary interest, the VFP equation is linearized and a set of coupled integral equations is semianalytically derived in terms of the density and energy modulations (Sec. III D). In Sec. III E we briefly introduce the numerical procedures for solving the integral equations. Having done these preparations, we illustrate in Sec. IV a recirculating IBS (RIBS) ring as an example [51], which was proposed to enhance the IBS effect as an alternative option to laser heating. The semianalytical calculations are benchmarked against particle tracking simulations using ELEGANT. The results and the model assumptions are compared and discussed in Sec. IV C and Sec. IV D, respectively. Finally we summarize the results and discuss possible future work in Sec. V.

II. INTRABEAM SCATTERING: COMPLETELY INTEGRATED MODIFIED PIWINSKI FORMALISM

A. Model assumptions

The main effect of IBS is to change in the six-dimensional (6-D) beam emittances. In the longitudinal direction, it is usually expressed in terms of the change of the uncorrelated energy spread (or slice energy spread). There are in general two theoretical frameworks to calculate IBS growth rates: Piwinski [56] and Bjorken and Mtingwa [57]. Based on collisional momentum kinematics, the former uses the classical Rutherford differential cross section between two test particles, then averages over scattering angles and all beam particles, calculates the mean change of the invariants, and eventually obtains the well-known Piwinski formulas, including the rise times of the transverse emittances and the longitudinal energy spread. The latter formalism, by Bjorken and Mtingwa, employs the time-evolution operator which relates the transition from an initial quantum state to the final quantum state of a physical scattering process, combines Feynman diagram technique to calculate the scattering amplitude, and eventually gives the Bjorken-Mtingwa formulas. Other methods to evaluate IBS growth rates can be based on direct numerical solutions of the Vlasov-Fokker-Planck (VFP) equation using Monte Carlo algorithm (see, for example, Ref. [58]) and so on. The full numerical simulation methods can be computationally expensive; all these methods however should lead to consistent results within certain common assumptions.

Here we use the completely integrated modified Piwinski formalism (CIMP) based on Kubo *et al.* [52], which is found to greatly reduce the computing time for IBS calculations and thus more easily and quickly to apply, while retains variation of lattice parameters in single-pass or recirculating beamlines. Several relevant model assumptions are summarized below: (1) the beam particles are nonrelativistic in the beam frame, while ultrarelativistic in the lab frame; (2) the 6-D beam phase space distribution is Gaussian, which is a practical approximation but not always valid, because an interplay of friction and diffusion may not allow for the beam distribution to remain Gaussian during the transport; (3) the transport line is assumed uncoupled. (4) Since the synchrotron motion is usually neglected in a single-pass accelerator, the following formulas for the longitudinal motion assume a coasting beam, resulting in an additional factor of 2 ahead of the longitudinal IBS growth rate [see Ref. [59] or Eq. (1) below]. (5) The average over circumference or path length in CIMP formulas will be removed for the single-pass accelerator and the Coulomb log factor takes into account the variation of optics functions along the beamline, i.e., the instantaneous IBS growth rates are evaluated.

B. Summary of CIMP formulas

In this subsection we will summarize the main results of Ref. [52] as the background information for our subsequent analysis. The rate of change of the uncorrelated energy spread due to IBS can be written as

$$\tau_{\mathrm{IBS},\delta}^{-1}=\frac{1}{\sigma_\delta}\frac{\mathrm{d}\sigma_\delta}{\mathrm{d}s}=2\times 2\pi^{3/2}A\left[\frac{\sigma_H^2}{\sigma_\delta^2}\left([\mathrm{Log}]_x\frac{g(\frac{b}{a})}{a}+[\mathrm{Log}]_y\frac{g(\frac{a}{b})}{b}\right)\right], \quad (1)$$

where a prefactor of 2 is due to lack of the synchrotron motion [59]. Note that we have changed the time derivative to the derivative with respect to the path coordinate s by $\tau_{\mathrm{IBS}}^{-1}[\mathrm{m}^{-1}]=\tau_{\mathrm{IBS}}^{-1}[\mathrm{sec}^{-1}]/c$.

The IBS growth rates for the transverse emittances are expressed as

$$\tau_{x,\mathrm{IBS}}^{-1}=\frac{1}{\epsilon_x^G}\frac{\mathrm{d}\epsilon_x^G}{\mathrm{d}s}=4\pi^{3/2}A\left[-a[\mathrm{Log}]_x g\left(\frac{b}{a}\right)+\frac{\mathcal{H}_x\sigma_H^2}{\epsilon_x^G}\left([\mathrm{Log}]_x\frac{g(\frac{b}{a})}{a}+[\mathrm{Log}]_y\frac{g(\frac{a}{b})}{b}\right)\right], \quad (2)$$

and

$$\tau_{y,\mathrm{IBS}}^{-1} = \frac{1}{\epsilon_y^G}\frac{\mathrm{d}\epsilon_y^G}{\mathrm{d}s} = 4\pi^{3/2}A\left[-b[\mathrm{Log}]_y g\left(\frac{a}{b}\right) + \frac{\mathcal{H}_y\sigma_H^2}{\epsilon_y^G}\left([\mathrm{Log}]_x\frac{g(\frac{b}{a})}{a} + [\mathrm{Log}]_y\frac{g(\frac{a}{b})}{b}\right)\right], \quad (3)$$

where the superscript G denotes the geometric emittances. In the above equations,

$$A = \frac{r_e^2 N}{64\pi^2\gamma^4\epsilon_x^G\epsilon_y^G\sigma_z^{\mathrm{rms}}\sigma_\delta} = \frac{I_b}{(2\sqrt{2\ln 2})64\pi^2\gamma^2\epsilon_x^N\epsilon_y^N\sigma_\delta}\frac{r_e^2}{ce}, \quad (4)$$

with r_e is the classical electron radius, c the speed of light, e the magnitude of the unit charge, N is the number of electrons per bunch, γ the Lorentz relativistic factor, $\epsilon_{x,y}^{N,G}$ the normalized (N) or geometric (G) transverse emittances [Note that $\epsilon_{x,y}^N = \beta\gamma\epsilon_{x,y}^G$ with β the normalized velocity.], σ_z^{rms} the rms bunch length (assuming Gaussian bunch), and σ_δ the relative uncorrelated (or slice) energy spread. In what follows, when dealing with phase space microbunched dynamics a coasting beam approximation will be made, and thus a factor of $2\sqrt{2\ln 2}$ is used to convert the rms Gaussian bunch length to an equivalent full width for uniform flattop bunch. In Eqs. (1) to (3), the Coulomb log factors $[\mathrm{Log}]_{x,y}$ are taken to be [52]

$$[\mathrm{Log}]_x = \ln\left(\frac{q^2}{a^2}\right) \quad (5a)$$

$$[\mathrm{Log}]_y = \ln\left(\frac{q^2}{b^2}\right) \quad (5b)$$

with $a = \frac{\sigma_H}{\gamma}\sqrt{\frac{\beta_x}{\epsilon_x^G}}$ and $b = \frac{\sigma_H}{\gamma}\sqrt{\frac{\beta_y}{\epsilon_y^G}}$, $\beta_{x,y}$ the Twiss or Courant-Snyder envelope function in the transverse horizontal and vertical plane [60]. In Eqs. (5), $q = \sigma_H\beta\sqrt{2d/r_e}$, d the maximum impact parameter, prescribed by $d = \min\{\sigma_x, \sigma_y, \lambda_D\}$, $\sigma_{x,y}$ the horizontal and vertical beam sizes. σ_H will be specified below. The factors $[\mathrm{Log}]_{x,y}$ typically range from 10 to 20. Based on the example that we will illustrate in Sec. IV, Fig. 1 shows the $[\mathrm{Log}]_{x,y}$ along the beamline, where $[\mathrm{Log}]_{x,y} \approx 12$–$16$, as expected. Typically the Coulomb log terms depend weakly on the arguments.

In Eqs. (1) to (3), the g function is defined as [61]

$$g(w) = \sqrt{\frac{\pi}{w}}\left[P_{-1/2}^0\left(\frac{w^2+1}{2w}\right) \pm P_{-1/2}^{-1}\left(\frac{w^2+1}{2w}\right)\right], \quad (6)$$

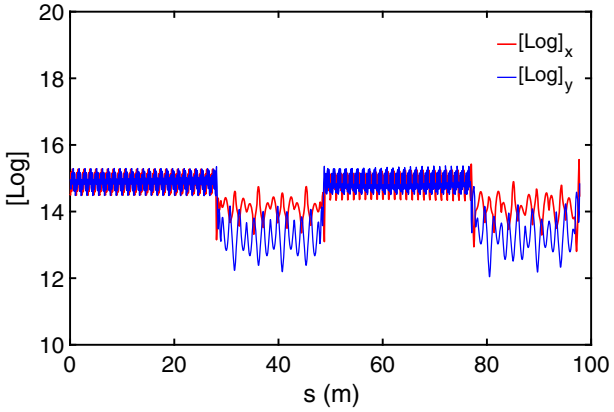

FIG. 1. Numerical values of the Coulomb log factors $[\mathrm{Log}]_{x,y}$ along s in a recirculating accelerator beamline. This quantities are defined in Eq. (5).

where $P_\nu^{-\mu}$ is the associated Legendre polynomial. For $w \geq 1$, the positive sign is taken; for $w \leq 1$, the negative sign is assigned. $g(w) \to \sqrt{\pi}$, as $w \to 1$. As suggested in Ref. [52], the numerical values of $g(w)$ have been benchmarked and the w dependence is shown in Fig. 2. Inside the squared brackets of Eqs. (1) to (3),

$$\frac{1}{\sigma_H^2} = \frac{1}{\sigma_\delta^2} + \frac{\mathcal{H}_x}{\epsilon_x^G} + \frac{\mathcal{H}_y}{\epsilon_y^G}, \quad (7)$$

where the dispersion invariants in the x and y directions are

$$\mathcal{H}_{x,y} = \gamma_{x,y}\eta_{x,y}^2 + 2\alpha_{x,y}\eta_{x,y}\eta'_{x,y} + \beta_{x,y}\eta'^2_{x,y} = \frac{R_{16,36}^2 + (\beta_{x,y}R_{26,46} + \alpha_{x,y}R_{16,36})^2}{\beta_{x,y}}, \quad (8)$$

with $\alpha_{x,y}$, $\beta_{x,y}$, $\gamma_{x,y}$ the Twiss or Courant-Snyder functions [60]. The R_{16} and R_{36} (or η_x, η_y) are, respectively, the horizontal and vertical dispersion functions, and R_{26} and

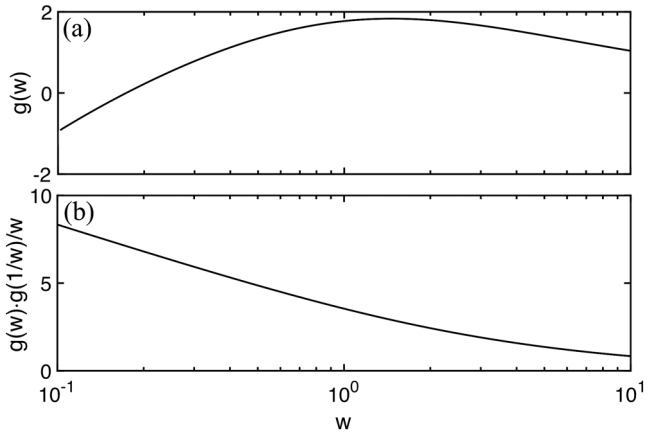

FIG. 2. (a) the scattering function $g(w)$ and (b) its product $g(w)g(1/w)/w$.

R_{46} (or η_x', η_y') are the corresponding derivatives with respect to the path coordinate s.

Note that the above equations are applicable to both round and flat beams (assuming Gaussian distribution). For a flat beam, e.g., $\sigma_y \ll \sigma_x$ (or $\epsilon_y \ll \epsilon_x$), the Coulomb log terms $[\mathrm{Log}]_x \geq [\mathrm{Log}]_y$, and can be pulled outside the square brackets, resulting in approximated Eqs. (38)–(41) in the Ref. [52]. For a round beam, also the case of our interest in this paper, $[\mathrm{Log}]_x \approx [\mathrm{Log}]_y$. In what follows, we will simply denote as [Log].

Before ending this section, we comment that, provided the Twiss or Courant-Snyder functions $\alpha_{x,y}$, $\beta_{x,y}$, $\gamma_{x,y}$ along a beamline, the numerical solutions of Eqs. (1) to (3) may be obtained by solving the difference equations in a small grid Δs. When advancing each Δs, the new beam emittances and energy spread should be updated until the end of the beamline. In Sec. IV we will illustrate for more details the numerical results based on a practical recirculating beamlime design.

III. PHASE SPACE EVOLUTION OF MICROBUNCHED BEAM

In the previous section we have summarized the IBS growth rates for the change of bulk beam parameters, including the uncorrelated beam emittances and the slice energy spread. In this section we will consider the phase space evolution of a phase space microbunched beam in the presence of both the collective interaction and incoherent IBS effects.

In the absence of collision, the phase space dynamics subject to collective interactions can be described by the 6-D collisionless Boltzmann equation or Vlasov equation (or Jeans equation) [62,63], which can be written as $\mathrm{d}f/\mathrm{d}s = 0$. The collective interactions may arise from beam-environment interactions, e.g., due to the beam pipe structure or surface roughness [64], or the beam itself, e.g., the space charge [12,65] or CSR [66–70]. It deserves here to clarify that, under framework of the 6-D phase space, the Coulomb interactions within a charged particle beam may be separated into two effects: one is the Liouvillian space charge force, associated with the collective interaction on a given test particle of the rest of the beam particles, and the other the scattering effect [71]. The scattering effect is further categorized into small-angle, multiple and large-angle, single scattering events. As mentioned in Sec. I, the multiple small-angle Coulomb scattering, or IBS, is of our current interest. By introducing the binary-encounter model [71], the phase space dynamics involving the scattering effect can be formulated as the VFP equation with the corresponding dynamic friction and diffusion coefficients. Therefore the Vlasov equation itself is no longer valid; an additional collision term should be added, i.e., $\mathrm{d}f/\mathrm{d}s = (\partial f/\partial s)_\mathrm{c}$ (where the subscript c denotes the collision).

In the following subsection, we first formulate the phase space dynamics in the beam rest frame, in which the momentum change of a test particle before and after a collision is described by a time-independent probability function, and derive the VFP equation. The corresponding dynamic friction and diffusion coefficients can be written as the Landau collision integrals [72]. Since we are primarily interested in the onset of MBI, we will linearize the VFP equation. For high-brightness electron beam, in the lab frame, the longitudinal beam emittance (or temperature) is usually much smaller (colder) than the transverse emittance (or temperature) [48,55], typically $T_\parallel/T_\perp \leq 10^{-4}$, so the friction and diffusion coefficients can be further simplified and analytically expressed in terms of beam quantities as a function of the path coordinate s. Having obtained the friction and diffusion coefficients, we will substitute them into the linearized VFP equation, and solve for the perturbed phase space distribution in the forms of the density and energy modulations. The resultant equations form a set of coupled linear integral equations.

A. Fokker-Planck formalism

The phase space distribution function $\mathcal{F}$ in the beam rest frame may be described as

$$\mathcal{F} = \mathcal{F}_\perp(\tilde{\mathbf{x}}_\perp, \tilde{\mathbf{p}}_\perp; \tilde{t})\mathcal{F}_\parallel(\tilde{z}, \tilde{p}_z; \tilde{t}), \tag{9}$$

where the position-momentum pairs $(\tilde{\mathbf{x}}_\perp, \tilde{\mathbf{p}}_\perp)$ and $(\tilde{z}, \tilde{p}_z)$ represent, respectively, the transverse 4-D and the longitudinal 2-D phase space coordinate at time $\tilde{t}$. These quantities with the tilde on top are denoted in the beam rest frame. The normalization condition is assumed to satisfy $\int \mathcal{F}\mathrm{d}\tilde{\mathbf{x}}_\perp \mathrm{d}\tilde{\mathbf{p}}_\perp \mathrm{d}\tilde{z}\mathrm{d}\tilde{p}_z = \mathcal{N}$, where $\mathcal{N}$ is the particle density in beam rest frame.

The kinetic equation for the phase space distribution in the presence of collision takes the general form

$$\frac{\mathrm{d}\mathcal{F}}{\mathrm{d}\tilde{t}} = \left(\frac{\partial \mathcal{F}}{\partial \tilde{t}}\right)_\mathrm{c}, \tag{10}$$

where the subscript c denotes the collision. Now we define $\psi(\tilde{\mathbf{p}}, \Delta\tilde{\mathbf{p}})$ as the probability that a particle of the momentum $\tilde{\mathbf{p}}$ acquires a change of $\Delta\tilde{\mathbf{p}}$ due to collision within a time interval $\Delta\tilde{t}$. The phase space distribution function at $\tilde{t}$, $\mathcal{F}(\tilde{\mathbf{r}}, \tilde{\mathbf{p}}; \tilde{t})$, may be expressed in terms of the phase space distribution at earlier time with the collision probability function

$$\mathcal{F}(\tilde{\mathbf{r}}, \tilde{\mathbf{p}}; \tilde{t}) = \int_{-\infty}^{\infty} \mathcal{F}(\tilde{\mathbf{r}}, \tilde{\mathbf{p}} - \Delta\tilde{\mathbf{p}}; \tilde{t} - \Delta\tilde{t})\psi(\tilde{\mathbf{p}} - \Delta\tilde{\mathbf{p}}, \Delta\tilde{\mathbf{p}})d\Delta\tilde{\mathbf{p}}. \tag{11}$$

Note that ψ is independent of time, meaning that the scattering event is assumed a Markov process. Further

assuming that the momentum change $\Delta\tilde{\mathbf{p}}$ is small compared with $\tilde{\mathbf{p}}$, one has

$$\left(\frac{\partial\mathcal{F}}{\partial\tilde{t}}\right)_c = \frac{1}{\Delta\tilde{t}}[\mathcal{F}(\tilde{\mathbf{r}},\tilde{\mathbf{p}};\tilde{t}) - \mathcal{F}(\tilde{\mathbf{r}},\tilde{\mathbf{p}};\tilde{t}-\Delta\tilde{t})] = \frac{1}{\Delta\tilde{t}}\left[-\sum_{i=1}\frac{\partial}{\partial\tilde{p}_i}(\mathcal{F}\langle\Delta\tilde{p}_i\rangle) + \frac{1}{2}\sum_{i,j}\frac{\partial^2}{\partial\tilde{p}_i\partial\tilde{p}_j}(\mathcal{F}\langle\Delta\tilde{p}_i\Delta\tilde{p}_j\rangle)\right], \tag{12}$$

in which $i,j = x,y,z$ and $\langle\cdots\rangle = \int_{-\infty}^{\infty}(\cdots)\psi(\tilde{\mathbf{p}},\Delta\tilde{\mathbf{p}})d\Delta\tilde{\mathbf{p}}$.

In Eq. (12), the first and the second term, defined as $\mathcal{D}_i = -\frac{1}{\Delta\tilde{t}}\langle\Delta\tilde{p}_i\rangle, \mathcal{D}_{ij} = \frac{1}{\Delta\tilde{t}}\langle\Delta\tilde{p}_i\Delta\tilde{p}_j\rangle$, are respectively interpreted as the friction and diffusion coefficients, which give the mean rate of changes due to multiple consecutive weak collisions [71,73]. Note that in Eq. (12) the two terms have the opposite sign. Under equilibrium conditions, the diffusion term in momentum space is balanced by the friction term, and there would be no net change on the phase space distribution function. Here we note that the interplay of the friction and the diffusion may not necessarily allow for the beam distribution to remain Gaussian. For single-pass or recirculating accelerators, where beam particles do not reach an equilibrium state, the exact form of the equilibrium distribution may not be our current interest; we are more interested in the dynamical evolution of a (given) unperturbed initial phase space distribution.

Now we consider the Coulomb scattering as a series of consecutive weak binary collisions, in the beam frame the corresponding friction and diffusion coefficients can be written as Landau collision integrals [55,72,73]

$$\mathcal{D}_z = -8\pi m_e e^4[\mathrm{Log}]\int \mathrm{d}^3\tilde{\mathbf{p}}'\mathcal{F}(\tilde{\mathbf{p}}')\frac{\tilde{p}_z - \tilde{p}'_z}{|\tilde{\mathbf{p}}-\tilde{\mathbf{p}}'|^3} \tag{13}$$

and

$$\mathcal{D}_{zz} = 4\pi m_e e^4[\mathrm{Log}] \times \int \mathrm{d}^3\tilde{\mathbf{p}}'\mathcal{F}(\tilde{\mathbf{p}}')\frac{(\tilde{\mathbf{p}}-\tilde{\mathbf{p}}')^2\delta_{ij} - (\tilde{p}_i - \tilde{p}'_i)(\tilde{p}_j - \tilde{p}'_j)}{|\tilde{\mathbf{p}}-\tilde{\mathbf{p}}'|^3}, \tag{14}$$

where m_e is the electron rest mass, [Log] is the Coulomb log, which can be determined by Eq. (5). From Eq. (10) and (12), the VFP equation can be written as

$$\frac{\mathrm{d}\mathcal{F}}{\mathrm{d}\tilde{t}} = -\sum_i\frac{\partial}{\partial\tilde{p}_i}(\mathcal{D}_i\mathcal{F}) + \frac{1}{2}\sum_{i,j}\frac{\partial^2}{\partial\tilde{p}_i\tilde{p}_j}(\mathcal{D}_{ij}\mathcal{F}). \tag{15}$$

where $i,j = x,y,z$. As discussed in the beginning of this section, the longitudinal beam temperature $T_\parallel = m_e c^2\sigma_\delta^2$ is much lower (colder) than the transverse temperature $T_\perp = m_e c^2\gamma^2\sigma_{x',y'}^2$, typically $T_\parallel/T_\perp \le 10^{-4}$; the IBS growth rate is much larger in the longitudinal direction than in the transverse directions [see Eqs. (1) to (3) or Fig. 5 below]. Therefore Eq. (15) can be simplified by integrating the coefficients over the transverse phase space

$$\frac{\mathrm{d}\mathcal{F}}{\mathrm{d}\tilde{t}} = -\frac{\partial}{\partial\tilde{p}_z}(\langle\mathcal{D}_z\rangle_\perp\mathcal{F}) + \frac{1}{2}\frac{\partial^2}{\partial\tilde{p}_z^2}(\langle\mathcal{D}_{zz}\rangle_\perp\mathcal{F}) \tag{16}$$

where $\langle\cdots\rangle_\perp \equiv \int(\cdots)\mathcal{F}_\perp(\tilde{\mathbf{x}}_\perp,\tilde{\mathbf{p}}_\perp;\tilde{t})\mathrm{d}\tilde{\mathbf{x}}_\perp\mathrm{d}\tilde{\mathbf{p}}_\perp$ and $\int\mathcal{F}_\perp(\tilde{\mathbf{x}}_\perp,\tilde{\mathbf{p}}_\perp;\tilde{t})\mathrm{d}\tilde{\mathbf{x}}_\perp\mathrm{d}\tilde{\mathbf{p}}_\perp = 1$. We note that the decomposition in Eq. (9) is consistent with the simplification made here.

Transformation of Eq. (16) back to the lab frame can be done by the following substitution [55]

$$\tilde{t}\to s/c\gamma, \quad \tilde{p}_z\to\Delta E/c\gamma, \quad \mathcal{F}\to f, \quad \mathcal{N}\to n_0/\gamma \tag{17}$$

and

$$\langle\mathcal{D}_z\rangle_\perp\to D_z, \qquad \langle\mathcal{D}_{zz}\rangle_\perp\to D_{zz}/c\gamma. \tag{18}$$

Then Eq. (16) becomes

$$\frac{\mathrm{d}f}{\mathrm{d}s} = -\frac{\partial}{\partial\delta}(D_z f) + \frac{D_{zz}}{2}\frac{\partial^2 f}{\partial\delta^2} \tag{19}$$

with the relative energy deviation $\delta = \Delta E/E_0$ (E_0 the reference energy). In Eq. (19) the diffusion coefficient is moved out from the energy derivative, as we will show in Sec. III C that it is independent of δ. The detailed derivation and explicit expressions of D_z and D_{zz} will be discussed in Sec. III C.

B. Linearized Vlasov-Fokker-Planck equation

Let us define the 6-D phase space distribution function, $f(\mathbf{X};s)$, where the phase space coordinate $\mathbf{X} = (x,x',y,y',z,\delta)^T = (\mathbf{X}_{4D},\mathbf{X}_{2D})^T$ with x,y, respectively, the transverse horizontal and vertical position, x',y' the transverse horizontal and vertical divergence, z the local bunch coordinate ($z>0$ for the bunch head), and δ the relative energy deviation. Notice that the VFP equation is essentially a nonlinear equation, because not only $\mathrm{d}f/\mathrm{d}s$, but also D_z and D_{zz} in general have f dependencies. It is therefore, either analytically or numerically, unlikely to obtain the direct, exact solution of 6-D phase space distribution to the VFP equation in a general transport line without any approximation. Since we are primarily interested in the onset of MBI, we shall linearize the VFP equation. Assume $f = f_0 + f_1$, where $|f_1| \ll f_0$ with the normalization $\int f(\mathbf{X};s)\mathrm{d}\mathbf{X} = n_0$ (n_0 is the particle density in the lab frame). After substituting $f = f_0 + f_1$ into Eq. (19), the zeroth-order equation becomes

$$\frac{df_0}{ds}=\frac{\partial f_0}{\partial s}+\frac{\partial f_0}{\partial x}\left(\frac{dx}{ds}\right)_0+\frac{\partial f_0}{\partial x'}\left(\frac{dx'}{ds}\right)_0+\frac{\partial f_0}{\partial y}\left(\frac{dy}{ds}\right)_0+\frac{\partial f_0}{\partial y'}\left(\frac{dy'}{ds}\right)_0. \tag{20}$$

In Eq. (20) we have neglected two terms: $\partial f_0/\partial z$ due to the coasting beam approximation and $(d\delta/ds)_0$ due to absence of collective interaction to the zeroth order. Notice that, on the right-hand side (rhs) of Eq. (20) [and Eqs. (21), (22) below], the subscripts 0 and 1 are used to denote the order for those quantities which depend on the bunch current density and are thus proportional to $f(=f_0+f_1)$.

Neglecting the second order and higher order terms, we obtain the first-order equation

$$\frac{df_1}{ds}=-\frac{\partial f_0}{\partial\delta}\left(\frac{d\delta}{ds}\right)_1-\frac{\partial}{\partial\delta}(D_{z,0}(s)f_1)-\frac{\partial}{\partial\delta}(D_{z,1}(s)f_0)+\frac{D_{zz,0}(s)}{2}\frac{\partial^2 f_1}{\partial\delta^2}+\frac{D_{zz,1}(s)}{2}\frac{\partial^2 f_0}{\partial\delta^2}, \tag{21}$$

where the left-hand side (lhs) is

$$\frac{df_1}{ds}=\frac{\partial f_1}{\partial s}+\frac{\partial f_1}{\partial x}\left(\frac{dx}{ds}\right)_0+\frac{\partial f_1}{\partial x'}\left(\frac{dx'}{ds}\right)_0+\frac{\partial f_1}{\partial y}\left(\frac{dy}{ds}\right)_0+\frac{\partial f_1}{\partial y'}\left(\frac{dy'}{ds}\right)_0+\frac{\partial f_1}{\partial z}\left(\frac{dz}{ds}\right)_0. \tag{22}$$

Notice that two terms are neglected: $(dx/ds)_1$ and $(dx'/ds)_1$ due to absence of transverse collective angular kick. The first term on rhs of Eq. (21) is responsible for the longitudinal collective interactions, where $(d\delta/ds)_1$ at $s=\tau$ can be explicitly expressed as [8,9,14]

$$\left(\frac{d\delta}{d\tau}\right)_1=-\frac{Nr_e}{\gamma}\int_{-\infty}^{\infty}\frac{d\kappa}{2\pi}Z_\parallel(\kappa;\tau)b(\kappa;\tau)e^{i\kappa z_\tau}. \tag{23}$$

where N is the total number of particles per bunch, $Z_\parallel(\kappa;\tau)$ is the impedance per unit length at $s=\tau$, $b(\kappa;\tau)$ is the density modulation or bunching factor, which will be defined later [see Eq. (41) below]. Combining Eqs. (21) and (22) and integrating over the path coordinate, we obtain the linearized VFP equation

$$f_1(\mathbf{X};s)=f_1(\mathbf{X};0)-\int_0^s\frac{\partial f_0}{\partial\delta}\left(\frac{d\delta}{d\tau}\right)_1d\tau-\int_0^s\left[\frac{\partial}{\partial\delta}(D_{z,0}(\tau)f_1)+\frac{\partial}{\partial\delta}(D_{z,1}(\tau)f_0)\right]d\tau+\int_0^s\left[\frac{D_{zz,0}(\tau)}{2}\frac{\partial^2 f_1}{\partial\delta^2}+\frac{D_{zz,1}(\tau)}{2}\frac{\partial^2 f_0}{\partial\delta^2}\right]d\tau. \tag{24}$$

From Eq. (24) one can see that the perturbed phase space distribution at a certain location s has three contributions made by the pure optics transport (the first term on rhs), the collective effects (the second term), and the incoherent IBS effects (the third and the fourth terms). Now we have derived the linearized VFP equation, Eq. (21) and (22), or its integral form, Eq. (24).

The initial unperturbed 6-D phase space distribution can be written as

$$f_0(\mathbf{X};0)=\frac{N}{(2\pi)^3\gamma^2\epsilon_x^N\epsilon_y^N\sigma_{z0}\sigma_{\delta0}}e^{-\frac{1}{2}\mathbf{X}_{4D,0}^T\Sigma_{4D,0}^{-1}\mathbf{X}_{4D,0}-\frac{z_0^2}{2\sigma_{z0}^2}-\frac{(\delta_0-hz_0)^2}{2\sigma_{\delta0}^2}}. \tag{25}$$

with h the energy chirp (energy-position correlation) of the bunch.

For modulation wavelengths much smaller than the electron bunch length, we may assume that the initial beam distribution is uniform in z (i.e., the coasting beam approximation) and Gaussian in the transverse phase space and longitudinal energy variables in the lab frame, i.e.,

$$f_0(\mathbf{X};0)=\frac{n_0}{(2\pi)^{5/2}\gamma^2\epsilon_x^N\epsilon_y^N\sigma_{\delta0}}e^{-\frac{1}{2}\mathbf{X}_{4D,0}^T\Sigma_{4D,0}^{-1}\mathbf{X}_{4D,0}-\frac{(\delta_0-hz_0)^2}{2\sigma_{\delta0}^2}}, \tag{26}$$

where n_0 is the particle density. Comparing with Eq. (25), $Ne^{-\frac{z_0^2}{2\sigma_{z0}^2}}/\sqrt{2\pi}\sigma_{z0}\to n_0$. The beam sigma matrix in the exponent

$$\Sigma_{4D,0}=\langle\mathbf{X}_{4D,0}\mathbf{X}_{4D,0}^T\rangle, \tag{27}$$

characterizes the beam second moments. For a transverse uncoupled (non-magnetized) beam, Eq. (26) can be separated into the x and y direction and parameterized using Twiss or Courant-Snyder parameters as

$$\mathbf{X}_{2D,x}^T\Sigma_{2D,x}^{-1}\mathbf{X}_{2D,x}=\frac{x_0^2+(\beta_{x0}x'_0+\alpha_{x0}x_0)^2}{\epsilon_{x0}^G\beta_{x0}}, \tag{28}$$

and similar for the y direction. Note that the determinant of the beam sigma matrix can be related to the beam emittance $\sqrt{\det(\Sigma_{2D,x})}=\epsilon_x^G$.

Together with the explicit expressions of the IBS friction and diffusion coefficients that we will derive in the next subsection, Eq. (24) will be used to derive the governing equations for the phase space density modulations.

C. Friction and diffusion coefficients

1. Derivation of diffusion coefficient

For convenience of the subsequent discussion, we may write the 6-D phase space coordinate in the beam rest frame as the position-momentum pair $(\tilde{\mathbf{r}},\tilde{\mathbf{p}})$, with $\tilde{\mathbf{r}}=(\tilde{x},\tilde{y},\tilde{z})$

and $\tilde{\mathbf{p}} = (\tilde{p}_x, \tilde{p}_y, \tilde{p}_z)$. In the beam rest frame, the beam distribution in the momentum space can be expressed in terms of the beam temperatures [55]

$$\mathcal{F} = \mathcal{F}_\perp(\tilde{\mathbf{p}}_\perp)\mathcal{F}_\parallel(\tilde{p}_z) = \frac{\mathcal{N}}{(2\pi m_e)T_\perp\sqrt{2\pi m_e T_\parallel}} e^{-\frac{\tilde{p}_x^2+\tilde{p}_y^2}{2m_e T_\perp}-\frac{\tilde{p}_z^2}{2m_e T_\parallel}}, \tag{29}$$

where $\mathcal{N}$ is the particle density in the beam frame. The relations between the beam temperature and the divergence are $T_\parallel = m_e c^2\sigma_\delta^2$ and $T_\perp = m_e c^2\gamma^2\sigma_{x',y'}^2$, where $\sigma_{x',y'}$ are the transverse horizontal and vertical angular divergences. Note that Boltzmann constant k_B has been absorbed in $T_\perp$ and $T_\parallel$ and not explicitly shown in our notation. In what follows we will substitute Eq. (29) into Eq. (14) to simplify the diffusion coefficient. To calculate the integral, we will use the following formula [55,74]

$$\frac{1}{R} = \sqrt{\frac{2}{\pi}}\int_0^\infty e^{-\frac{\xi^2}{2}R^2}\mathrm{d}\xi. \tag{30}$$

The denominator of the integrand in Eq. (14), in the limit of $T_\parallel \ll T_\perp$, can be approximated as $|\tilde{\mathbf{p}}-\tilde{\mathbf{p}}'|^3 \approx [(\tilde{p}_x-\tilde{p}'_x)^2+(\tilde{p}_y-\tilde{p}'_y)^2]^{3/2}$. Using the approximate form and Eq. (30), Eq. (14) can be integrated over $\tilde{\mathbf{p}}'_\perp$ analytically,

$$\begin{aligned}
&\int \mathrm{d}^2\tilde{\mathbf{p}}'_\perp \frac{\mathcal{F}_\perp(\tilde{\mathbf{p}}'_\perp)}{\sqrt{(\tilde{p}_x-\tilde{p}'_x)^2+(\tilde{p}_y-\tilde{p}'_y)^2}} \\
&= \sqrt{\frac{2}{\pi}}\int_0^\infty\int \mathcal{F}_\perp(\tilde{\mathbf{p}}'_\perp)e^{-\frac{\xi^2}{2}[(\tilde{p}_x-\tilde{p}'_x)^2+(\tilde{p}_y-\tilde{p}'_y)^2]}\mathrm{d}^2\tilde{\mathbf{p}}'_\perp\mathrm{d}\xi \\
&= \frac{\mathcal{N}}{\sqrt{2\pi m_e T_\perp}}\int_0^\infty \frac{e^{-\frac{\zeta}{(\zeta+1)}\frac{\tilde{p}_x^2+\tilde{p}_y^2}{2m_e T_\perp}}}{\sqrt{\zeta}(\zeta+1)}\mathrm{d}\zeta
\end{aligned} \tag{31}$$

where the dummy variable $\zeta = \xi^2 m_e T_\perp$ is introduced. Here and in what follows, we will suppress the upper $+\infty$ and lower $-\infty$ integration limits if not specified.

Next, we evaluate the averaged diffusion coefficient in the beam rest frame

$$\langle\mathcal{D}_{zz}\rangle_\perp = \int \mathcal{D}_{zz}\mathcal{F}_\perp(\tilde{\mathbf{p}}_\perp)\mathrm{d}\tilde{\mathbf{p}}_\perp, \tag{32}$$

with $\mathcal{F}_\perp(\tilde{\mathbf{p}}_\perp) = \frac{\mathcal{N}}{2\pi m_e T_\perp}e^{-\frac{\tilde{p}_x^2+\tilde{p}_y^2}{2m_e T_\perp}}$ [Eq. (29)]. Putting Eqs. (14) and (31) together, one can obtain

$$\begin{aligned}
\langle\mathcal{D}_{zz}\rangle_\perp &= 4\pi m_e e^4[\mathrm{Log}]\frac{1}{\sqrt{2\pi m_e T_\perp}} \\
&\times\int_0^\infty \frac{1}{\sqrt{\zeta}(1+2\zeta)}\mathrm{d}\zeta = \frac{2\pi^{\frac{3}{2}}\mathcal{N}m_e e^4[\mathrm{Log}]}{\sqrt{m_e T_\perp}}.
\end{aligned} \tag{33}$$

Using Eqs. (17), (18) and $T_\perp = m_e c^2\gamma^2\sigma_{x',y'}^2$, the above equation can be transformed back to the lab frame in terms of the beam current $I_b/I_A = 4\pi\sigma_\perp^2 r_e n_0$ [55]

$$D_{zz} = \frac{\sqrt{\pi}}{2}\left(\frac{r_e[\mathrm{Log}]}{\gamma^2\epsilon_\perp^N\sigma_\perp}\frac{I_b}{I_A}\right), \tag{34}$$

where $\epsilon_\perp^N = \sqrt{\epsilon_x^N\epsilon_y^N} = \gamma\sqrt{\sigma_x\sigma_{x'}\sigma_y\sigma_{y'}}$, $\sigma_\perp = \sqrt{\sigma_x\sigma_y}$, and $I_A = mc^3/e \approx 17045$ A.

2. Derivation of friction coefficient

In this subsection we will follow similar procedures outlined in Sec. III C 1 to derive the friction coefficient. Unlike the previous case, we write the denominator of the integrand in Eq. (13) in the exact form $|\tilde{\mathbf{p}}-\tilde{\mathbf{p}}'|^3 = [(\tilde{p}_x-\tilde{p}'_x)^2+(\tilde{p}_y-\tilde{p}'_y)^2+(\tilde{p}_z-\tilde{p}'_z)^2]^{3/2}$.

To evaluate the integration in Eq. (13), we use another useful integration formula [74]

$$\frac{1}{R^{\frac{3}{2}}} = \frac{1}{4\sqrt{\pi}}\int_0^\infty \sqrt{\xi}e^{-\frac{\xi}{4}R}\mathrm{d}\xi. \tag{35}$$

With Eq. (35), the integration in Eq. (13) over $\tilde{\mathbf{p}}'_\perp$ can be made analytically,

$$\begin{aligned}
&\int \mathrm{d}^2\tilde{\mathbf{p}}'_\perp\mathcal{F}_\perp(\tilde{\mathbf{p}}'_\perp)\int \mathrm{d}\tilde{p}'_z\frac{(\tilde{p}_z-\tilde{p}'_z)\mathcal{F}_\parallel(\tilde{p}'_z)}{[(\tilde{p}_x-\tilde{p}'_x)^2+(\tilde{p}_y-\tilde{p}'_y)^2+(\tilde{p}_z-\tilde{p}'_z)^2]^{3/2}}, \\
&= \int \mathrm{d}^2\tilde{\mathbf{p}}'_\perp\mathcal{F}_\perp(\tilde{\mathbf{p}}'_\perp)\int_0^\infty\frac{\sqrt{\lambda}}{4\sqrt{\pi}}\int \mathrm{d}\tilde{p}'_z(\tilde{p}_z-\tilde{p}'_z)\mathcal{F}_\parallel(\tilde{p}'_z)e^{-\frac{\lambda}{4}[(\tilde{p}_x-\tilde{p}'_x)^2+(\tilde{p}_y-\tilde{p}'_y)^2+(\tilde{p}_z-\tilde{p}'_z)^2]}\mathrm{d}\lambda, \\
&= \tilde{p}_z\sqrt{\frac{2}{\pi}}\int_0^\infty\frac{\sqrt{\lambda}e^{-\frac{\lambda}{2}\left(\frac{\tilde{p}_x^2+\tilde{p}_y^2}{2+m_e T_\perp\lambda}+\frac{\tilde{p}_z^2}{2+m_e T_\parallel\lambda}\right)}}{(2+m_e T_\perp\lambda)(2+m_e T_\parallel\lambda)^{3/2}}\mathrm{d}\lambda.
\end{aligned} \tag{36}$$

Similarly, we can evaluate the averaged friction coefficient in the beam rest frame, $\langle \mathcal{D}_z \rangle_\perp = \int \mathcal{D}_z \mathcal{F}_\perp(\tilde{\mathbf{p}}_\perp) \mathrm{d}\tilde{\mathbf{p}}_\perp$. Letting $\rho = m_e T_\parallel \lambda$, we have $m_e T_\perp \lambda = (\frac{T_\perp}{T_\parallel})\rho \gg \rho$. Putting Eqs. (13) and (36) together, one may obtain

$$\begin{aligned}\langle \mathcal{D}_z \rangle_\perp &= -8\pi \mathcal{N} m_e e^4 [\mathrm{Log}] \frac{\tilde{p}_z}{\sqrt{2\pi}(m_e T_\parallel \lambda)^{3/2}} \\ &\quad \times \int_0^\infty \frac{\sqrt{\rho} e^{-\frac{\rho}{2+\rho}\left(\frac{\tilde{p}_z^2}{2m_e T_\parallel}\right)}}{(1+\frac{T_\perp}{T_\parallel}\rho)(2+\rho)^{3/2}} \mathrm{d}\rho \\ &\approx -8\pi \mathcal{N} m_e e^4 [\mathrm{Log}] \frac{\tilde{p}_z}{\sqrt{2\pi}(m_e T_\parallel \lambda)^{3/2}} \\ &\quad \times \frac{T_\parallel}{T_\perp} \int_0^\infty \frac{e^{-\frac{\rho}{2+\rho}\left(\frac{\tilde{p}_z^2}{2m_e T_\parallel}\right)}}{\sqrt{\rho}(2+\rho)^{3/2}} \mathrm{d}\rho \\ &= -\frac{4\pi \mathcal{N} e^4 [\mathrm{Log}]}{T_\perp} \mathrm{erf}\left(\frac{\tilde{p}_z}{\sqrt{2 m_e T_\parallel}}\right), \end{aligned} \tag{37}$$

where the assumption $T_\parallel \ll T_\perp$ has been used. Similarly, using Eqs. (17), (18), $T_\perp = m_e c^2 \gamma^2 \sigma_{x',y'}^2$ and $T_\parallel = m_e c^2 \sigma_\delta^2$, the above equation can be transformed back to the lab frame in terms of the beam current

$$D_z = -\left(\frac{r_e [\mathrm{Log}]}{\gamma^2 \epsilon_\perp^{N^2}} \frac{I_b}{I_A}\right) \mathrm{erf}\left(\frac{\delta}{\sqrt{2}\sigma_\delta}\right). \tag{38}$$

The IBS dynamics involves small-angle, multiple particle scattering, and the physical meanings of the friction and diffusion are similar to particle scattering in plasma [73]. The friction term would decelerate or accelerate the local particles, depending on the energy deviation δ [see, e.g., Eq. (38), noting that the error function is an odd function], and tend to reach the central reference energy. In contrast, the diffusion term [Eq. (34)] would tend to expand the local particles.

Before ending this subsection, it deserves here to summarize the main results obtained in Sec. III B and Sec. III C. Assuming that the beam phase space distribution is Gaussian and $T_\parallel \ll T_\perp$, we have obtained the friction and diffusion coefficients, expressed in the lab frame, respectively,

$$D_z = -\left(\frac{r_e [\mathrm{Log}]}{\gamma^2 \epsilon_\perp^{N^2}} \frac{I_b}{I_A}\right) \mathrm{erf}\left(\frac{\delta}{\sqrt{2}\sigma_\delta}\right) = D_{z,0} + D_{z,1}, \tag{39}$$

and

$$D_{zz} = \frac{\sqrt{\pi}}{2}\left(\frac{r_e [\mathrm{Log}]}{\gamma^2 \epsilon_\perp^N \sigma_\perp} \frac{I_b}{I_A}\right) = D_{zz,0} + D_{zz,1}. \tag{40}$$

In what follows, when dealing with phase space density modulations, the bunch current I_b will consist of two parts: the average current and the modulated current, i.e., $I_b = \bar{I}_b + \Delta I_b = \bar{I}_b(1 + \frac{\Delta n}{n_0})$, where the modulated current is proportional to the density modulation. For convenience, we may write the friction and diffusion coefficients in Eqs. (39) and (40) as a sum of the averaged (with subscript 0) and the modulated (with subscript 1) quantities.

D. Governing integral equations

In the above subsections we have already prepared all the ingredients for the semianalytical formulation of the phase space microbunched dynamics, including the linearized VFP equation [Eq. (24)] and the explicit expressions of the friction and diffusion coefficients [Eq. (39) and (40)]. To obtain the dynamical equations of the phase space modulations, let us define the density modulation (or, bunching factor) as

$$b(k_z; s) = \frac{1}{N}\int f_1(\mathbf{X}; s) e^{-ik_z z_s} \mathrm{d}\mathbf{X} = \frac{n_0}{N}\int \frac{\Delta n(z_s)}{n_0} e^{-ik_z z_s} \mathrm{d}z, \tag{41}$$

where k_z is the modulation wave number, i.e., $k_z = 2\pi/\lambda$ with λ the (initial) modulation wavelength, and the energy modulation

$$\begin{aligned} p(k_z; s) &= \frac{1}{N}\int \delta_s f_1(\mathbf{X}; s) e^{-ik_z z_s} \mathrm{d}\mathbf{X} \\ &= \frac{n_0}{N}\int \Delta\delta(z_s) e^{-ik_z z_s} \mathrm{d}z, \end{aligned} \tag{42}$$

with $\Delta\delta = \delta_s - hz$. For simplicity, we only consider the case with $h = 0$, i.e., without bunch compression. It is straightforward to extend the following formulation to $h \neq 0$ case by introduction of the bunch compression factor $C(s) = [1 - hR_{56}(s)]^{-1}$. We further assume that the initial perturbed phase space distribution consists of density modulation only, i.e., [see also Eq. (26)]

$$f_1(\mathbf{X}; 0) = \frac{\Delta n}{n_0} f_0(\mathbf{X}; 0). \tag{43}$$

By multiplying $\frac{1}{N} e^{-ik_z z_s}$ on both sides of Eq. (24) and integrating over the 6-D phase space coordinate, one can obtain the following integral equation for the density modulation [see also Eq. (41)]

$$b(k_z;s)=\frac{1}{N}\int f_1(\mathbf{X};0)e^{-ik_z(s)z_s}\mathrm{d}\mathbf{X}-\frac{1}{N}\int_0^s ik_z(\tau)R_{56}(\tau\to s)\int f_0(\mathbf{X};\tau)\left(\frac{\mathrm{d}\delta}{\mathrm{d}\tau}\right)_1 e^{-ik_z(s)z_s(\tau)}\mathrm{d}\mathbf{X}\mathrm{d}\tau$$
$$-\frac{1}{N}\int_0^s ik_z(s)R_{56}(\tau\to s)\int (D_{z,0}(\tau)f_1(\mathbf{X};\tau)+D_{z,1}(\tau)f_0(\mathbf{X};\tau))e^{-ik_z(s)z_s(\tau)}\mathrm{d}\mathbf{X}\mathrm{d}\tau$$
$$-\frac{1}{N}\int_0^s k_z^2(s)R_{56}^2(\tau\to s)\int\left(\frac{D_{zz,0}(\tau)}{2}f_1(\mathbf{X};\tau)+\frac{D_{zz,1}(\tau)}{2}f_0(\mathbf{X};\tau)\right)e^{-ik_z(s)z_s(\tau)}\mathrm{d}\mathbf{X}\mathrm{d}\tau, \tag{44}$$

where the integration of δ by parts has been applied for those terms with $R_{56}(\tau\to s)$. The first term on the rhs can be evaluated analytically, i.e.,

$$\frac{1}{N}\int\frac{\Delta n(z_s)}{n_0}f_0(\mathbf{X};0)e^{-ik_z(s)z_s}\mathrm{d}\mathbf{X}_0=b(k_z;0)\{\mathrm{L.D.};0,s\}\equiv b_0(k_z;s). \tag{45}$$

For simplicity and clarity, we shall introduce a set of symbolic expressions here and the following. In Eq. (45), $\{\mathrm{L.D.};0,s\}$ characterizes the phase space smearing (or Landau damping)

$$\{\mathrm{L.D.};0,s\}=\exp\left\{-\frac{k_z^2(s)}{2}\begin{bmatrix}\epsilon_{x0}^G\beta_{x0}\left(R_{51}(s)-\frac{\alpha_{x0}}{\beta_{x0}}R_{52}(s)\right)^2+\frac{\epsilon_{x0}^G}{\beta_{x0}}R_{52}^2(s)\\ +\epsilon_{y0}^G\beta_{y0}\left(R_{53}(s)-\frac{\alpha_{y0}}{\beta_{y0}}R_{54}(s)\right)^2+\frac{\epsilon_{y0}^G}{\beta_{y0}}R_{54}^2(s)+\sigma_{\delta0}^2R_{56}^2(s)\end{bmatrix}\right\}. \tag{46}$$

For the second term on the rhs of Eq. (44), the integral inside $\mathrm{d}\tau$ can be done using the method of characteristics. This integration has been performed in many literatures (see, e.g., Refs. [8,9,14,37] for the detailed derivation), and here we only quote the result

$$\int_0^s ik_z(\tau)R_{56}(\tau\to s)\int f_0(\mathbf{X};\tau)\left(\frac{\mathrm{d}\delta}{\mathrm{d}\tau}\right)_1 e^{-ik_z(s)z_s(\tau)}\mathrm{d}\mathbf{X}\mathrm{d}\tau=-\int_0^s ik_z(s)R_{56}(\tau\to s)\frac{\bar{I}_b(\tau)}{\gamma I_A}Z_\parallel(k_z;\tau)\{\mathrm{L.D.};\tau,s\}Nb(k_z;\tau)\mathrm{d}\tau, \tag{47}$$

where $Z_\parallel(k_z;\tau)$ is the impedance per unit length at $s=\tau$, describing the collective interactions. $R_{56}(\tau\to s)$ can be obtained through extracting the element on the fifth row and the sixth column of the following matrix operation

$$\mathbf{R}(\tau\to s)=\mathbf{R}^{-1}(\tau)\mathbf{R}(s). \tag{48}$$

or explicitly written as

$$R_{56}(\tau\to s)=R_{56}(s)-R_{56}(\tau)+R_{51}(\tau)R_{52}(s)-R_{51}(s)R_{52}(\tau)+R_{53}(\tau)R_{54}(s)-R_{53}(s)R_{54}(\tau). \tag{49}$$

Note that when $\tau=s$, $R_{56}(\tau\to s)=0$. In Eq. (47), we introduce the phase space smearing term [cf. Eq. (46)]

$$\{\mathrm{L.D.};\tau,s\}=\exp\left\{-\frac{k_z^2(s)}{2}\begin{bmatrix}\epsilon_x^G\beta_{x0}\left(R_{51}(\tau,s)-\frac{\alpha_{x0}}{\beta_{x0}}R_{52}(\tau,s)\right)^2+\frac{\epsilon_x^G}{\beta_{x0}}R_{52}^2(\tau,s)\\ +\epsilon_y^G\beta_{y0}\left(R_{53}(\tau,s)-\frac{\alpha_{y0}}{\beta_{y0}}R_{54}(\tau,s)\right)^2+\frac{\epsilon_y^G}{\beta_{y0}}R_{54}^2(\tau,s)+\sigma_\delta^2R_{56}^2(\tau,s)\end{bmatrix}\right\} \tag{50}$$

where $R_{5j}(\tau,s)=R_{5j}(s)-R_{5j}(\tau)$, $j=1,2,3,4,6$. When $\tau=0$, $R_{5j}(0,s)=R_{5j}(s)$.

As will be demonstrated in Sec. IV, the impedance per unit length of the steady-state free-space CSR can be written as [66–68]

$$Z_{\parallel,\mathrm{CSR}}(k_z;s)=-iA\frac{k_z^{1/3}(s)}{|\rho(s)|^{2/3}} \tag{51}$$

where ρ is the (local) radius of curvature of the dipole, $A=-2\pi[\mathrm{Bi}'(0)/3+i\mathrm{Ai}'(0)]\approx-0.94+1.63i$ with Ai' and Bi' are the first derivative of Airy functions [74]. The CSR expression, Eq. (51), is valid when the beam energy is ultrarelativistic,

the transverse beam size satisfies the so-called Derbenev criterion $\kappa = \sigma_\perp/\lambda^{2/3}\rho^{1/3} < 1$ [75], and the modulation wavelength must be small compared with a threshold dimension of beam pipe [14], i.e., $\lambda < \lambda_{\rm th} = \frac{2\pi}{k_{\rm th}}$, with $k_{\rm th} = \sqrt{\frac{2\rho}{3}(\frac{\pi}{h})^3}$ (h the full height of the beam pipe).

In addition to the CSR, the steady-state free-space longitudinal space charge (LSC) effect may be of interest [12],

$$Z_{\parallel,\rm LSC}(k_z;s) = \frac{4i}{\gamma r_b}\frac{1-\xi_b K_1(\xi_b)}{\xi_b} \tag{52}$$

where K_1 is the modified Bessel function of the second kind, $r_b = 1.747\times(\sigma_x+\sigma_y)/2$ is the weighted average radius of the beam [76] and $\xi_b = k_z r_b/\gamma$. Equation (52) is valid when $\lambda > 4\pi r_b/\gamma$.

For a more complete collection of CSR impedance models, including the entrance and exit transient CSR effects, and the LSC impedance models, we refer the interested reader to Ref. [14] and references therein.

For the third term on the rhs of Eq. (44), responsible for the IBS friction effect, we need to evaluate two integrals. Assume that the term involving f_1 can be written as a sum of the density and energy modulations

$$f_1(\mathbf{X};\tau) = \left[\frac{\Delta n(z_\tau)}{n_0} + \frac{\delta_\tau \Delta\delta(z_\tau)}{\sigma_{\delta\tau}^2}\right] f_0(\mathbf{X};\tau), \tag{53}$$

where the subscript τ denotes those quantities at $s=\tau$. Here we remind the reader that Eq. (53) may not be the most general expression; we have neglected possible phase space modulations that may emerge in the transverse or the transverse-longitudinal dimensions [14,77]. It has been found that for a long beam transport line (a long section linac or multi-pass recirculating accelerator), an intuitive way of quantifying MBI by successive multiplication of individual density modulation gains from subsections of a beamline is found to underestimate the effect [77]. In our following discussion, we always perform the start-to-end analysis; this ensures that Eq. (53) is valid in this situation.

By substituting Eq. (53) into the third term on the rhs of Eq. (44), the term with $D_{z,0}f_1$ is further split into two parts. These integrals, albeit the calculation is somewhat lengthy, can be evaluated analytically and summarized in Appendix A1, specifically Eqs. (A4) and (A7). For the fourth term on the rhs of Eq. (44), responsible for the IBS diffusion effect, the detailed derivation is similar and would not be presented in this paper. The resulting expressions are also summarized in Appendix A1, specifically Eqs. (A11) and (A12).

For the moment we have completed Eq. (44), i.e., the governing equation of the density modulation. Collection of Eqs. (45), (47), (A1), (A4), (A7), and (A10)–(A12) will give the resultant integral equation for $b(k_z;s)$. The complete expression is summarized in Appendix 2.

By multiplying $\frac{1}{N}\delta_s e^{-ik_z z_s}$ on both sides of Eq. (24) and integrating over the 6-D phase space coordinate, as has been done in Eq. (44), one can obtain the following integral equation for the energy modulation [see also Eq. (42)]

$$\begin{aligned} p(k_z;s) = {} & p_0(k_z;s) - \frac{1}{N}\int_0^s\int f_0(\mathbf{X};\tau)[ik_z(s)R_{56}(\tau\to s)\delta_\tau]\left(\frac{\mathrm{d}\delta}{\mathrm{d}\tau}\right)_1 e^{-ik_z(s)z_s(\tau)}\mathrm{d}\mathbf{X}\mathrm{d}\tau \\ & + \frac{1}{N}\int_0^s\int (D_{z,0}(\tau)f_1(\mathbf{X};\tau) + D_{z,1}(\tau)f_0(\mathbf{X};\tau))[ik_z(s)R_{56}(\tau\to s)\delta_\tau]e^{-ik_z(s)z_s(\tau)}\mathrm{d}\mathbf{X}\mathrm{d}\tau \\ & - \frac{1}{N}\int_0^s ik_z(s)R_{56}(\tau\to s)\int\left(\frac{D_{zz,0}(\tau)}{2}f_1(\mathbf{X};\tau) + \frac{D_{zz,1}(\tau)}{2}f_0(\mathbf{X};\tau)\right)[2-ik_z(s)R_{56}(\tau\to s)\delta_\tau]e^{-ik_z(s)z_s(\tau)}\mathrm{d}\mathbf{X}\mathrm{d}\tau. \end{aligned} \tag{54}$$

In order to perform the above integrations, one can follow the similar procedures to evaluation of Eq. (44), as outlined above. We skip the lengthy but straightforward derivations and only present the resulting integral equation for the energy modulation $p(k_z;s)$ in Appendix A2.

We have thus far obtained the coupled linear integral equations for the density and energy modulations, Eqs. (A13) and (A14). To further simplify the expressions we introduce several shorthand notations in Appendix A3. The governing integral equations for the density and energy modulations, $b(k_z;s)$, $p(k_z;s)$, can be rewritten in a simpler form

$$\begin{aligned} b(k_z;s) = {} & b_0(k_z;s) + i\int_0^s K^{(1)}_{Z_\parallel}(\tau,s)b(k_z;\tau)\mathrm{d}\tau + \int_0^s K^{(1)}_{\mathrm{IBS},z}(\tau,s)b(k_z;\tau)\mathrm{d}\tau + i\int_0^s K^{\perp(0)}_{\mathrm{IBS},z}(\tau,s)p(k_z;\tau)\mathrm{d}\tau \\ & - 2\int_0^s K^{(2)}_{\mathrm{IBS},zz}(\tau,s)b(k_z;\tau)\mathrm{d}\tau + i\int_0^s K^{(3)}_{\mathrm{IBS},zz}(\tau,s)p(k_z;\tau)\mathrm{d}\tau \end{aligned} \tag{55}$$

and

$$
\begin{aligned}
p(k_z;s) = p_0(k_z;s) &- \int_0^s [K^{(0)}_{Z_\parallel}(\tau,s) - K^{(2)}_{Z_\parallel}(\tau,s)\sigma^2_{\delta\tau}]b(k_z;\tau)\mathrm{d}\tau + i\int_0^s K^{(0)}_{\mathrm{IBS},z}(\tau,s)b(k_z;\tau)\mathrm{d}\tau \\
&+ 2i\int_0^s K^{\perp(1)}_{\mathrm{IBS},z}(\tau,s)b(k_z;\tau)\mathrm{d}\tau - \int_0^s K^{\perp(0)}_{\mathrm{IBS},z}(\tau,s)p(k_z;\tau)\mathrm{d}\tau + \int_0^s K^{\perp(2)}_{\mathrm{IBS},z}(\tau,s)p(k_z;\tau)\mathrm{d}\tau \\
&- 4i\int_0^s K^{(1)}_{\mathrm{IBS},zz}(\tau,s)b(k_z;\tau)\mathrm{d}\tau + 2i\int_0^s K^{(3)}_{\mathrm{IBS},zz}(\tau,s)\sigma^2_{\delta\tau}b(k_z;\tau)\mathrm{d}\tau \\
&- 3\int_0^s K^{(2)}_{\mathrm{IBS},zz}(\tau,s)p(k_z;\tau)\mathrm{d}\tau + \int_0^s K^{(4)}_{\mathrm{IBS},zz}(\tau,s)\sigma^2_{\delta\tau}p(k_z;\tau)\mathrm{d}\tau
\end{aligned} \tag{56}
$$

with

$$b_0(k_z;s) = b_0(k_z;0)\{\mathrm{L.D.};0,s\} \tag{57a}$$

$$p_0(k_z;s) = -ik_z(s)R_{56}(s)\sigma^2_{\delta\tau}b_0(k_z;0)\{\mathrm{L.D.};0,s\}. \tag{57b}$$

In the absence of IBS, those kernel functions K_{IBS} vanish and the above integral equations reduce to the familiar ones [37]. Since the integral equations are linear, we may collect those terms involving the density modulations, separate from the remaining energy modulations, and express in a matrix equation in the most compact form.

E. Numerical procedures for solving the integral equations

In this subsection we will present a general numerical procedure for solving the integral equation of Volterra type. Then we apply it to solve Eqs. (55) and (56).

A linear Volterra integral equation of the second kind may be written as

$$b(s) = b_0(s) + \int_0^s K(\tau,s)b(\tau)\mathrm{d}\tau \tag{58}$$

or split into the discrete sum as [78]

$$b(s_i) = b_0(s_i) + \Delta s\left(\frac{1}{2}K(0,s_i) + \sum_{j=1}^{i-1} K(u_j,s_i)b(u_j)\right), \tag{59}$$

for $s_i = s_0 + i\Delta s$ and $u_j = u_0 + j\Delta s$ being the grid points along the beam path, with i and j the grid indexes [not to be confused with the imaginary unit]. Here Δs is the grid spacing, s_0 and u_0 the initial positions. Here we assume $s_0 = u_0 = 0$. Equation (59) can be expressed in a matrix form

$$
\begin{bmatrix} b(s_1) \\ b(s_2) \\ b(s_3) \\ b(s_4) \\ \vdots \\ b(s_{N-1}) \\ b(s_N) \end{bmatrix}
=
\begin{bmatrix} b_0(s_1) \\ b_0(s_2) \\ b_0(s_3) \\ b_0(s_4) \\ \vdots \\ b_0(s_{N-1}) \\ b_0(s_N) \end{bmatrix}
+ \Delta s
\begin{pmatrix}
0 & & & & & 0 \\
\frac{1}{2}K(s_2,s_1) & 0 & & & & \\
\frac{1}{2}K(s_3,s_1) & K(s_3,s_2) & 0 & & & \\
\frac{1}{2}K(s_4,s_1) & K(s_4,s_2) & K(s_4,s_3) & 0 & & \\
\vdots & \vdots & \vdots & \vdots & & \\
\frac{1}{2}K(s_{N-1},s_1) & K(s_{N-1},s_2) & K(s_{N-1},s_3) & \cdots & 0 & \\
\frac{1}{2}K(s_N,s_1) & K(s_N,s_2) & K(s_N,s_3) & \cdots & K(s_N,s_{N-1}) & 0
\end{pmatrix}
\begin{bmatrix} b(s_1) \\ b(s_2) \\ b(s_3) \\ b(s_4) \\ \vdots \\ b(s_{N-1}) \\ b(s_N) \end{bmatrix}
\tag{60}
$$

or in shorthand notation

$$\mathbf{b} = \mathbf{b}_0 + \mathbf{K}\mathbf{b}. \tag{61}$$

Therefore, solving a linear integral equation may become to find the inverse of the matrix $(\mathcal{I} - \mathbf{K})$, with $\mathcal{I}$ the identity matrix. An alternative method may resort to numerical iterations, from which the order of iteration signifies the multistage microbunching amplification [9,79]. The number of numerical grid points must be ensured that the results are converged in the presence of both the collective interaction and IBS effects.

Now let us write Eqs. (55) and (56) in the matrix form as

$$\begin{pmatrix} \mathcal{P} & \mathcal{Q} \\ \mathcal{R} & \mathcal{S} \end{pmatrix} \begin{bmatrix} \mathbf{b}_{k_z} \\ \mathbf{p}_{k_z} \end{bmatrix} = \begin{bmatrix} \mathbf{b}_0 \\ \mathbf{p}_0 \end{bmatrix}. \tag{62}$$

Since the block matrices $\mathcal{P}$, $\mathcal{Q}$, $\mathcal{R}$, and $\mathcal{S}$ do not explicitly depend on $\mathbf{b}_{k_z}$ and $\mathbf{p}_{k_z}$, the solution can always be expressed as

$$\mathbf{b}_{k_z} = \mathcal{A}\mathbf{b}_0 + \mathcal{B}\mathbf{p}_0, \tag{63a}$$

$$\mathbf{p}_{k_z} = \mathcal{C}\mathbf{b}_0 + \mathcal{D}\mathbf{p}_0, \tag{63b}$$

where

$$\mathcal{A} = \mathcal{P}^{-1}[\mathcal{I} + \mathcal{Q}(\mathcal{S} - \mathcal{R}\mathcal{P}^{-1}\mathcal{Q})^{-1}\mathcal{R}\mathcal{P}^{-1}], \tag{64a}$$

$$\mathcal{B} = -\mathcal{P}^{-1}\mathcal{Q}(\mathcal{S} - \mathcal{R}\mathcal{P}^{-1}\mathcal{Q})^{-1}, \tag{64b}$$

$$\mathcal{C} = -(\mathcal{S} - \mathcal{R}\mathcal{P}^{-1}\mathcal{Q})^{-1}\mathcal{R}\mathcal{P}^{-1}, \tag{64c}$$

$$\mathcal{D} = (\mathcal{S} - \mathcal{R}\mathcal{P}^{-1}\mathcal{Q})^{-1}. \tag{64d}$$

In Eq. (64), $\mathcal{P}$, $\mathcal{Q}$, $\mathcal{R}$, $\mathcal{S}$ can be related to the kernel functions as [see Eqs. (A17) and (A18)]

$$\mathcal{P} = \mathcal{I} - i\mathcal{K}^{(1)}_{Z_\parallel} - \mathcal{K}^{(1)}_{\mathrm{IBS},z} + 2\mathcal{K}^{(2)}_{\mathrm{IBS},zz}, \tag{65a}$$

$$\mathcal{Q} = -i\mathcal{K}^{\perp(0)}_{\mathrm{IBS},z} - i\mathcal{K}^{(3)}_{\mathrm{IBS},zz}, \tag{65b}$$

$$\mathcal{R} = \mathcal{K}^{(0)}_{Z_\parallel} - \mathcal{K}^{(2)}_{Z_\parallel}\sigma^2_{\delta\tau} - i\mathcal{K}^{(0)}_{\mathrm{IBS},z} - 2i\mathcal{K}^{(1)}_{\mathrm{IBS},z} + 4i\mathcal{K}^{(1)}_{\mathrm{IBS},zz} - 2i\mathcal{K}^{(3)}_{\mathrm{IBS},zz}\sigma^2_{\delta\tau}, \tag{65c}$$

$$\mathcal{S} = \mathcal{I} + \mathcal{K}^{\perp(0)}_{\mathrm{IBS},z} - \mathcal{K}^{\perp(2)}_{\mathrm{IBS},z} + 3\mathcal{K}^{(2)}_{\mathrm{IBS},zz} - \mathcal{K}^{(4)}_{\mathrm{IBS},zz}\sigma^2_{\delta\tau}. \tag{65d}$$

where $\mathcal{I}$ is the identity matrix. When the IBS is absent, $\mathcal{Q}$ vanishes and $\mathcal{S} = \mathcal{I}$. In this special case, substitution of Eqs. (65) into Eqs. (64) gives an equivalent expression to Eq. (55) of Ref. [37].

To solve the coupled linear integral equations become to find the matrices $\mathcal{A}$, $\mathcal{B}$, $\mathcal{C}$, $\mathcal{D}$ or equivalently $\mathcal{P}$, $\mathcal{Q}$, $\mathcal{R}$, $\mathcal{S}$. To evaluate the matrix elements in Eqs. (65), the beam second moments in the kernel functions [beam emittances $\epsilon_{x,y}$ and energy spread σ_δ] should be updated based on Eqs. (1) to (3) with IBS effects included. We will discuss more details in Sec. IV when a practical example of a recirculating beamline will be presented. As for numerical evaluation of the confluent hypergeometric function [Eqs. (A18)], when the third argument is small, we may use the following useful approximation [18]

$${}_1F_1\left(-\frac{\nu^2}{4\delta};\beta;\delta\right) \approx \Gamma(\beta)\left(\frac{\nu}{2}\right)^{1-\beta} J_{\beta-1}(\nu), \tag{66}$$

where Γ is the Gamma function and $J_{\beta-1}$ is the Bessel function of the first kind [80]. Equation (66) can be further simplified to be the relevant forms

$${}_1F_1\left(\epsilon;\frac{1}{2};\delta\right) \approx \cos\nu \quad \text{and} \quad {}_1F_1\left(\epsilon+1;\frac{3}{2};\delta\right) \approx \mathrm{sinc}(\nu). \tag{67}$$

Using Eq. (67), the confluent hypergeometric functions in Eq. (A18) can be approximated to

$${}_1F_1\left(n+\frac{3}{2};\frac{1}{2};-\frac{1}{2}k_z^2(s)R_{56}^2(\tau\to s)\sigma^2_{\delta\tau}\right) \approx \cos(\sqrt{2n+3}k_z(s)R_{56}(\tau\to s)\sigma_{\delta\tau}), \tag{68a}$$

$${}_1F_1\left(n+\frac{5}{2};\frac{3}{2};-\frac{1}{2}k_z^2(s)R_{56}^2(\tau\to s)\sigma^2_{\delta\tau}\right) \approx \mathrm{sinc}(\sqrt{2n+5}k_z(s)R_{56}(\tau\to s)\sigma_{\delta\tau}). \tag{68b}$$

Figure 3 shows the dependence of the aforementioned two confluent hypergeometric functions on the third argument and comparison with their respective approximate forms. It can be seen that Eqs. (68) are good approximations within $|x| \ll 1$. In practical situations, $|x| = \frac{1}{2}k_z^2(s)R_{56}^2(\tau\to s)\sigma^2_{\delta\tau} \le 0.1$.

Before ending this section we summarize that the linearized VFP equation, in its differential form [Eq. (21)] or integral form [Eq. (24)], with the corresponding friction and diffusion coefficients [Eqs. (39) and (40), respectively] are

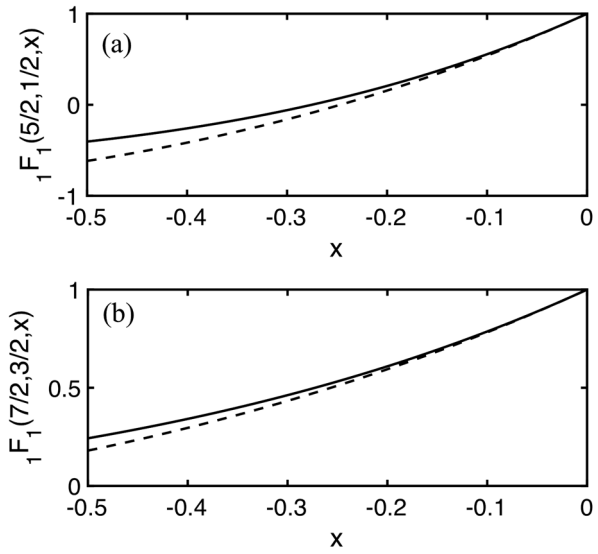

FIG. 3. The confluent hypergeometric functions (solid lines) and their small-argument approximation (dashed lines).

TABLE I. Initial electron beam and lattice parameters for recirculating IBS ring.

Name	Value	Unit
Beam energy	150	MeV
Average bunch current	62	A
Relative slice energy spread	1.13×10^{-5}	
Transverse normalized emittance	0.4, 0.4	μm
Initial beta function, $\beta_{x0,y0}$	0.36, 0.22	m
Initial alpha function, $\alpha_{x0,y0}$	−1.82, 1.33	

obtained. Instead of directly solving the linearized VFP, we derive the governing equations of the microbunched phase space distribution, including the density and energy modulations. The IBS effects reflect in two ways: the inflation changes of the transverse beam emittances and the energy spread via the phase space smearing or Landau damping [Eqs. (46), (50), (A5), and (A9)], evaluated based on the CIMP formulas [Eqs. (1) to (3)], and the dynamic friction and diffusion coefficients, determined by Eq. (A16).

IV. EXAMPLE: A LOW-ENERGY RECIRCULATING RING

In this section we would illustrate a recirculating IBS (RIBS) ring as a practical application to the developed semi-analytical formulation. The RIBS ring [51] was designed to enhance the IBS effects as an alternative option to laser heating, in order to increase the slice energy spread (while maintain high-quality phase space distribution) to suppress microbunching in the downstream transport line up to the undulator entrance. Having briefly described the lattice information (IV A) and outlined the numerical settings in particle tracking simulation (IV B), the semi-analytical calculations would be benchmarked against particle tracking simulations using ELEGANT. The results and the model assumptions are then compared and discussed in Sec. IV C and Sec. IV D, respectively.

A. Recirculating IBS ring

The lattice design of the RIBS ring is adopted from Ref. [51]. Table I lists the initial beam and lattice parameters. Such a recirculating beamline is composed of two identical low-beta focusing-drift-defocusing-drift (FODO) channels and two identical 180-degree quasi-isochronous achromatic arcs, as shown in Fig. 4(a). In the straight sections, the design value of the rms beam size is about 20 μm, corresponding to betatron function about 0.3 m [see Fig. 4(b)]. A smaller betatron envelope function might be achievable, e.g., down to a few mm, but the stronger quadrupole strengths may result in undesired optical aberrations. The straight-section lattice configuration ensures a standard technical design of the quadrupole magnets and negligible emittance growth in the presence of optical aberrations [51]. The optics design for the achromatic and quasi-isochronous arc is based on Ref. [81]; the dispersion and the momentum compaction functions are illustrated in Fig. 4(c). Between the straight and arc sections, additional quadrupole magnets are used to match the transient optics. Regarding the RIBS ring and the

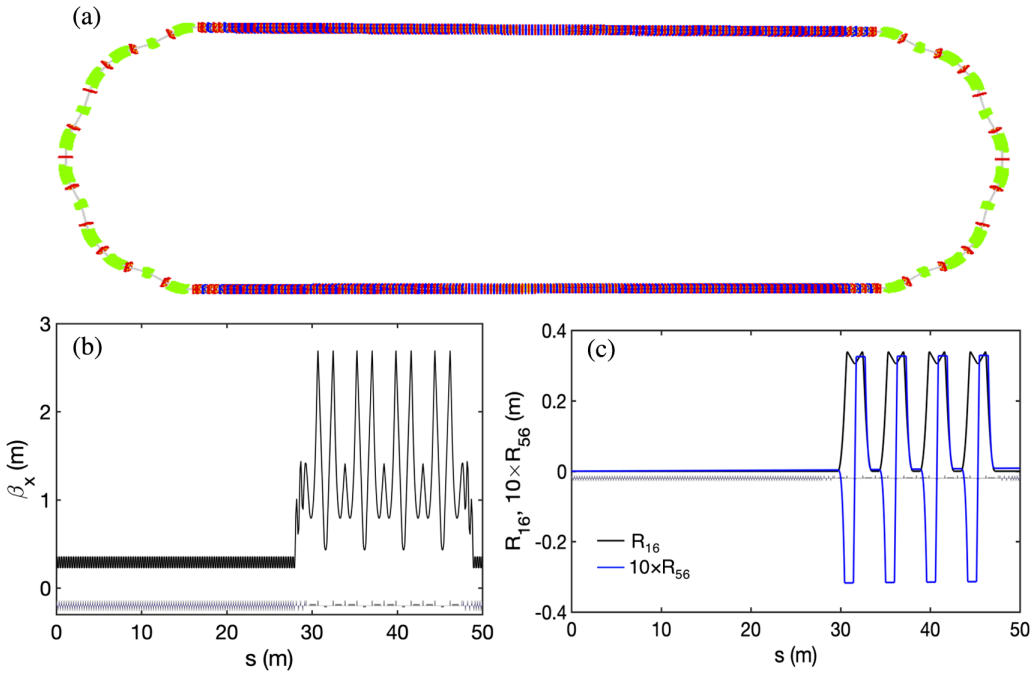

FIG. 4. (a) Schematic layout of the recirculating IBS ring, where dipoles are marked as green, focusing quadrupoles as red, and defocusing quadrupoles as blue. (b) Courant-Snyder envelope function. (c) Dispersion R_{16} and momentum compaction R_{56} functions.

TABLE II. Numerical setting used in ELEGANT tracking simulations.

Name	Value	Unit
Number of macroparticles	128×10^6	
Number of CSR bins	9000	
Number of macroparticles per bin	7000	
Number of CSR kicks	400	
Number of IBS bins	30	
Density modulation amplitude	0.01%	
Modulation wavelength	125	μm
Simulated uniform flattop duration	16/4800	ps/μm
Number of modulations atop	38	

estimate of the beam parameters, the readers are referred to Ref. [51] for more details.

B. Numerical settings for particle tracking simulations and data postprocessing

Before presenting the tracking simulation results, some remarks deserve to be made here on the numerical settings relevant to MBI and IBS and data postprocessing in ELEGANT [53,54]. Table II summarizes the converged numerical parameters used in preparation of the initial 6-D phase space distribution of macroparticles, in setting up the steady-state CSR effect within bending magnets (CSRCSBEND) [82] and the IBS effect along the beamline (IBSCATTER) [83]. Here we note that in particle tracking simulations, due to a limited number of simulation particles, the numerical settings for binning and filtering of numerical noise play an important role in the evaluation of MBI, especially when the microbunching amplification gain is high. In general, more simulation particles ensure lower numerical fluctuations (noise), and thus increasing the number of simulation particles will tend to converge the results. To compare with the linear theory at the onset of MBI, the initially imposed density modulation needs to be small enough to remain in the linear regime while such modulation should be large enough to rise above the numerical noises [13,14]. In ELEGANT simulations, we have simulated using 32, 64, and 128 millions of macroparticles and found that 64 or 128 millions of particles with density modulations smaller than 0.025% would give almost the same (converged) results. Furthermore, since the theoretical formulation assumes single-frequency modulation, the cutoff frequency is set up to the second harmonics [40]. The interested readers are referred to Refs. [14,40,82,84] for more details about the numerical settings.

As for setting the number of IBS bins, we set a criterion that this number should not be larger than the number of modulation wavelengths on top of the particle phase space distributions. This restriction can avoid emergence of nonphysical phase space modulations when ELEGANT redistributes the simulation particles after an IBS kick.

In postprocessing of particle tracking simulation data for analysis of MBI, to obtain the density modulation [cf. Eq. (41)], we make a histogram of the 6-D particle phase space distribution at a certain location over z (or t), and then take fast Fourier transform (FFT) on the histogram. The density modulation amplitude can be extracted from the modular amplitude of FFT at the corresponding modulation frequency. About histogram binning, we vary and choose at least five bins within a modulation wavelength to ensure that a complete modulation wavelength can be sampled, while not too many in order to avoid high-frequency noise when performing FFT. Another way to obtain the density modulation amplitude is to perform a sinusoidal fit, from which the fitting amplitude is the density modulation amplitude. To estimate the energy modulation amplitude [cf. Eq. (42)], the longitudinal beam phase space distribution (z, δ) is first sliced to obtain the mean energy within each slice, and a linear (or quadratic) polynomial fit is used to remove the residual linear (or quadratic) energy chirp. For each modulation period, the peak and valley are identified and the energy modulation amplitude can be calculated by averaging over the modulation periods.

C. Semianalytical calculation and particle tracking simulation results

In this subsection, we shall present the semi-analytical calculations and ELEGANT tracking simulation results for the RIBS ring outlined in Sec. IV A. Figure 5 displays the evolution of the IBS growth rates for the beam slice energy spread and the transverse slice emittance along the beamline. In ELEGANT, the IBS growth rates are calculated slice by slice based on Bjorken and Mtingwa formula [57]. In the following simulations, the number of IBS bins is chosen 30. From Fig. 5 we can see that both the CIMP [52] and ELEGANT give the consistent results, though in the first straight section the growth rate for the energy spread predicted by CIMP is a bit lower than that by ELEGANT.

Figure 6 illustrates the dynamic friction and diffusion coefficients along the beamline. Although it appears that $D_{\mathrm{IBS},z}$ is two orders of magnitude larger than $D_{\mathrm{IBS},zz}$, the dependence of $D_{\mathrm{IBS},z}$ on δ via the error function [see Eq. (A.16)] is not included in the figure. Within the core of the beam energy distribution, the effect of IBS friction is in fact smaller than IBS diffusion.

Figure 7 demonstrates the evolution of phase space microbunching along the beamline at the modulation wavelength $\lambda = 125$ μm, including the density and energy modulations. In Fig. 7(a) the microbunching density gain $G(s)$ is defined as the ratio of density modulation amplitudes at a certain location s to that at the initial location [see Eq. (41)], or

$$G(s) = \left| \frac{b(k_z; s)}{b(k_z; 0)} \right|. \tag{69}$$

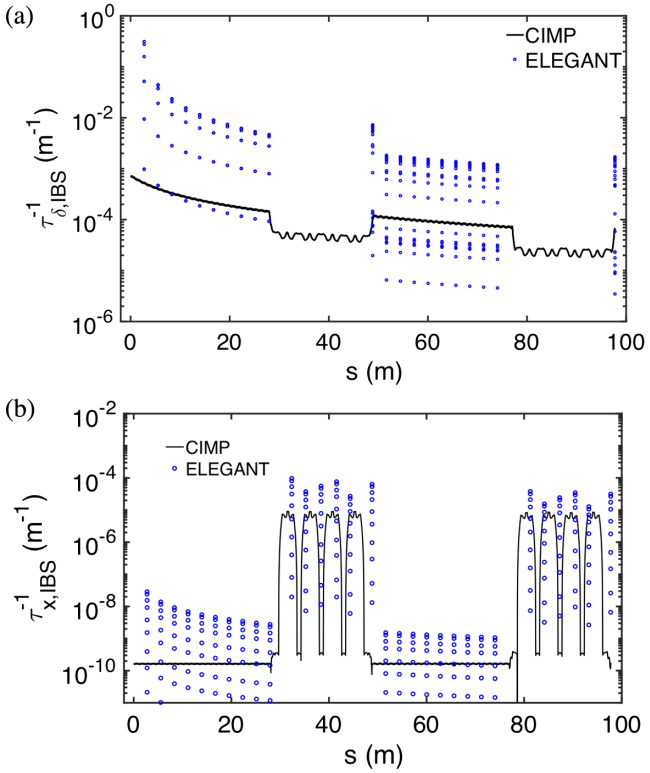

FIG. 5. The calculated IBS growth rates along the recirculating beamline for (a) slice energy spread, and (b) the transverse horizontal emittance. The solid lines are from CIMP model and the blue dots are from ELEGANT through IBSCATTER element [83]. There is a total of 30 blue dots at a certain location s, corresponding to the number of IBS bins [see Table II].

It can be seen that the density gain becomes much higher in the second arc than in the first arc, showing a significant gain enhancement. Note that the maximum gain in the first arc (around $s = 45$ m) is only 20. Since only the steady-state CSR is taken into account, there is no gain enhancement in the two straight sections. An intuitive estimate of the overall gain may be 400. However the information of the phase space microbunching residing in (x, z) or (x', z)

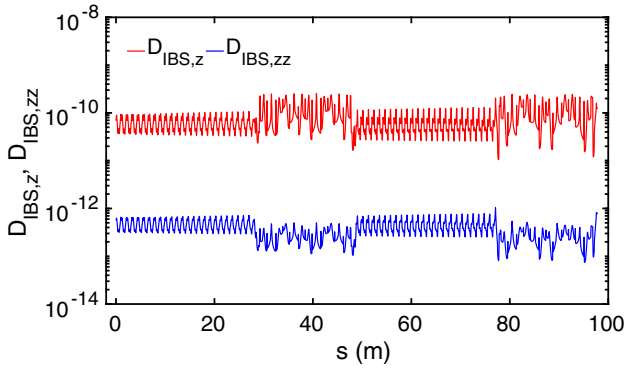

FIG. 6. The calculated IBS friction and diffusion coefficients [see also Eqs. (A.16)].

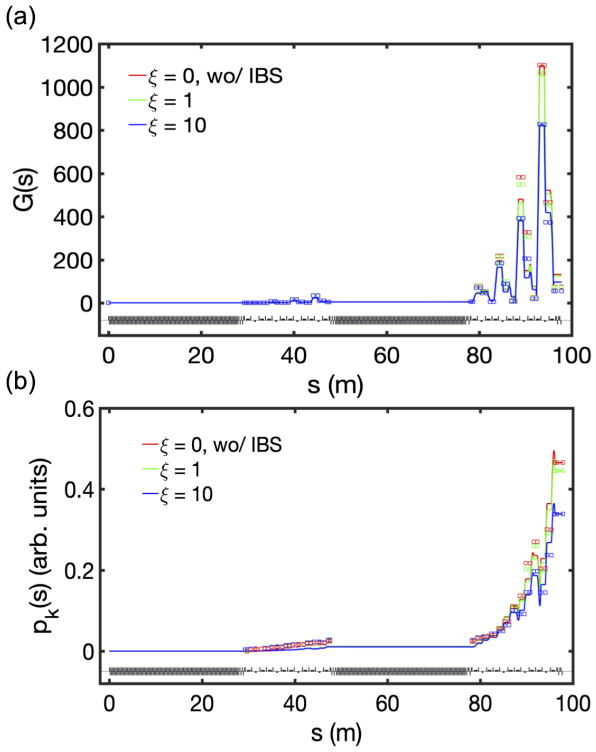

FIG. 7. (a) Gain functions $G(s)$, Eqs. (70) and (84), as a function of s, for $\lambda = 125$ μm. (b) Energy modulation, Eq. (56), as a function of s, for $\lambda = 125$ μm. Only the steady-state CSR is included in the cases. The red with $\xi = 0$ corresponds to the case without IBS; the green $\xi = 1$ includes the normal IBS effect; the blue $\xi = 10$ means the enhanced IBS inflation effect [see Eq. (70)]. In ELEGANT simulations, marked as square symbols, the initial modulation amplitude is set 0.01% and a total of 128-million macroparticles are used. Here we comment that, for the case with CSR and IBS, the tracking simulations may take about 10 hours using a 24-core computer, while obtaining the solid lines only takes within 5 minutes.

dimension, which is not accounted for by the naive estimate, will carry on growing and converting to the density or energy modulations downstream to the second arc [77]. In this regard, the start-to-end analysis is necessary and important to accurately evaluate the microbunching amplification.

The energy modulation plotted in Fig. 7(b) is in unit of the initial density modulation. Note that here in our calculation the initial phase space microbunching consists only the density modulation. Therefore such an energy modulation is primarily induced by CSR. In the presence of both initial density and energy modulations, one should append the additional contributions of $b_0(k_z; s)$ and $p_0(k_z; s)$ to Eqs. (45) and (57). The interested readers should be referred to Ref. [77] for more details. From Fig. 7, we clearly see that both the semianalytical calculations (solid lines) and the particle tracking simulations (squares) are in good agreement. For convenience of the following discussion with IBS, let us introduce an

enhancement factor $\xi \geq 0$, such that the relevant parameters to IBS will scale as [see also Eqs. (1) to (3) and (39), (40)]

$$\begin{Bmatrix} D_z \\ D_{zz} \\ \tau_{\delta,\mathrm{IBS}}^{-1} \\ \tau_{x,\mathrm{IBS}}^{-1} \\ \tau_{y,\mathrm{IBS}}^{-1} \end{Bmatrix} \rightarrow \xi \times \begin{Bmatrix} D_z \\ D_{zz} \\ \tau_{\delta,\mathrm{IBS}}^{-1} \\ \tau_{x,\mathrm{IBS}}^{-1} \\ \tau_{y,\mathrm{IBS}}^{-1} \end{Bmatrix}. \tag{70}$$

The trivial case with $\xi = 0$ corresponds to the absence of IBS. The case with $\xi = 1$ refers to the normal IBS effect, and $\xi > 1$ the enhanced IBS effect. As can be seen in Fig. 7, the normal IBS effect on MBI is negligibly small along the beamline, except for the locations where the gain is high, for example, at $s = 88$ or 93 m for the density gain and at slightly delayed locations for the energy modulation. The $\xi = 10$ case is also shown in this figure, where both semianalytical and tracking results agree, and indicates further gain reduction due to the enhanced IBS effect. The small gain reduction is expected, as IBS can be considered a slow diffusion process and the illustrated density gain only evolves in a single turn.

Demonstrated above is the evolution of phase space microbunching along the beamline at a certain modulation wavelength. The spectral response to MBI can be presented by scanning a range of modulation wavelengths, i.e., the gain spectrum at a particular location of the beamline.

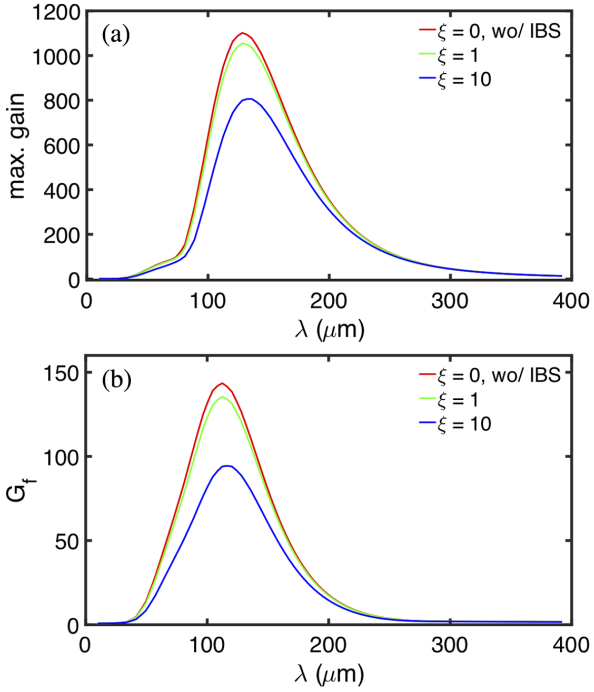

FIG. 8. Gain spectrum for (a) the maximum gain and (b) the gain at the exit of the recirculating beamline. Only the steady-state CSR is included in the cases.

Figure 8 illustrates the gain spectrum at $s = 93$ m (where the maximum gains occur) and at the exit of the beamline (the final gains, G_f). The shorter wavelengths enhance the phase space smearing (or Landau damping), while the longer wavelengths feature a negligible CSR effect. Although the IBS effect itself is small for a single turn, we can still see that the gain reduction due to IBS is more effective in the high-gain spectral region.

To further benchmark the theoretical formulation and gain a deeper understanding of the interplay between IBS and collective effects on phase space microbunching, a preliminary study may be conducted to investigate how the IBS scaling factor ξ affects MBI for a single turn. Figure 9 compares the semianalytical calculation with ELEGANT tracking for different IBS enhancement factors, including the maximum gain and the final gain for $\lambda = 125$ μm. From Fig. 9(a) it is evident that the beam emittances $\epsilon_{x,y}$ and slice energy spread σ_δ in Eqs. (46), (50), (A5), and (A9) should be updated based on the inflating IBS effect [determined by Eqs. (1) to (3)] to obtain the consistent results to particle

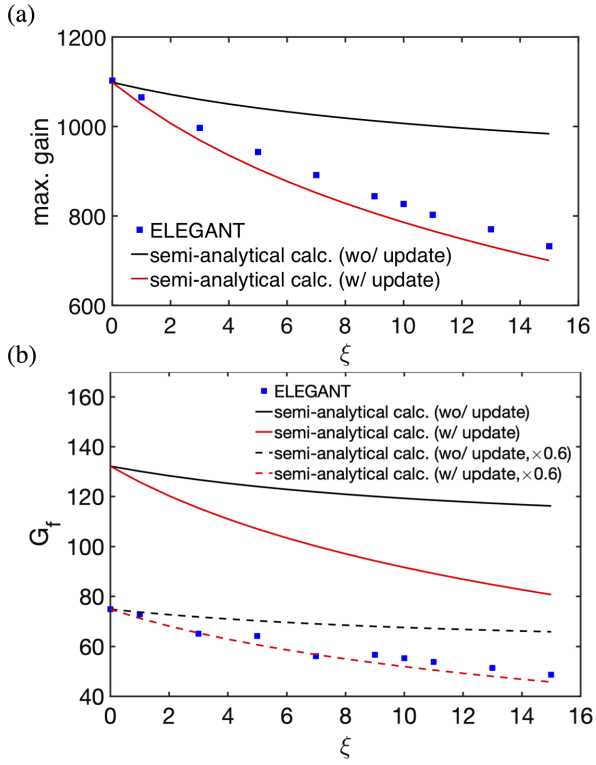

FIG. 9. Dependence of (a) the maximum gain and (b) the final gain on the IBS enhancement factor ξ. Only the steady-state CSR is included in the calculation. The solid lines are from semianalytical calculations and the square dots from ELEGANT tracking simulations. The black and red solid lines are, respectively, without and with update of σ_δ and $\epsilon_{x,y}$ due to IBS along the beamline. The black and red dashed lines in (b) are 0.6 times their corresponding solid lines. It can be seen that the red lines match well with the particle tracking results. For detailed discussion of the dashed lines, see comments in the context.

tracking simulations. Update of the only IBS-induced energy spread will result in underestimate of the IBS effect and thus giving a higher microbunching gain. As for the relevance of the friction and diffusion terms of the IBS dynamics to the overall microbunching gain, we use the developed semianalytical Vlasov solver to perform a numerical experiment, and find that the contribution of the friction term is in general small compared with that of the diffusion term. For the present example at 125 μm, let us consider four cases: (a) IBS off; (b) IBS on, with both $D_{\mathrm{IBS},z}$, $D_{\mathrm{IBS},zz}$; (c) IBS on, with only $D_{\mathrm{IBS},zz}$; (d) IBS on, with only $D_{\mathrm{IBS},z}$. In the comparisons, the IBS-induced growths of the slice energy spread and emittances remain the same for the cases. The difference only goes to the presence/absence of the friction and diffusion terms in the dynamical equations [Eqs. (63)–(65)]. It turns out that for cases (b)–(d) there is about $3 \sim 5\%$ gain reduction, compared with the case (a). With IBS, the difference between case (b) and (c) is much smaller (smaller than 0.1%), while the difference between (c) and (d) is about 1% in the gain reduction. We note that, since the friction and diffusion effects are not purely additive, a fair comparison should be made with respect to the absence of IBS [i.e., case (a)]. The exact numerical factor of gain reduction may vary for different beam parameters and different lattice designs. In our experience, the additional Landau damping due to IBS is stronger (primarily the slice energy spread increase, then the emittance growth) than the diffusion-induced gain reduction, followed by the friction-induced gain reduction.

Before ending this subsection, here we briefly conclude that the semianalytical and particle tracking results quantitatively agree to each other for the maximum microbunching gain [Fig. 9(a)], while in qualitative agreement to each other for the final gain in the presence of both normal and enhanced IBS effects [Fig. 9(b)]. In fact, the reduction of ELEGANT results [blue square dots in Fig. 9(b)] is due to gain saturation at the modulation wavelength in particle tracking simulations. This will be discussed in more detail in the next subsection.

D. Discussions

In the previous subsection, although a good agreement has been found in Fig. 9(a), a persistent reduction of the final gain in Fig. 9(b) does still exist. Having carefully checked our semianalytical code and the numerical parameters in ELEGANT, we find that the reduction is indeed due to gain saturation at the modulation wavelength and the second-harmonic modulation emerges near the exit of the beamline. To verify this, let us first take a look at the time-domain bunch current density distribution. Figure 10 illustrates the bunch histograms, with the average background being removed, at three different locations. For comparison, we have used a sinusoidal fit (blue lines) with a fixed wavelength $\lambda = 125$ μm to overlap the raw data

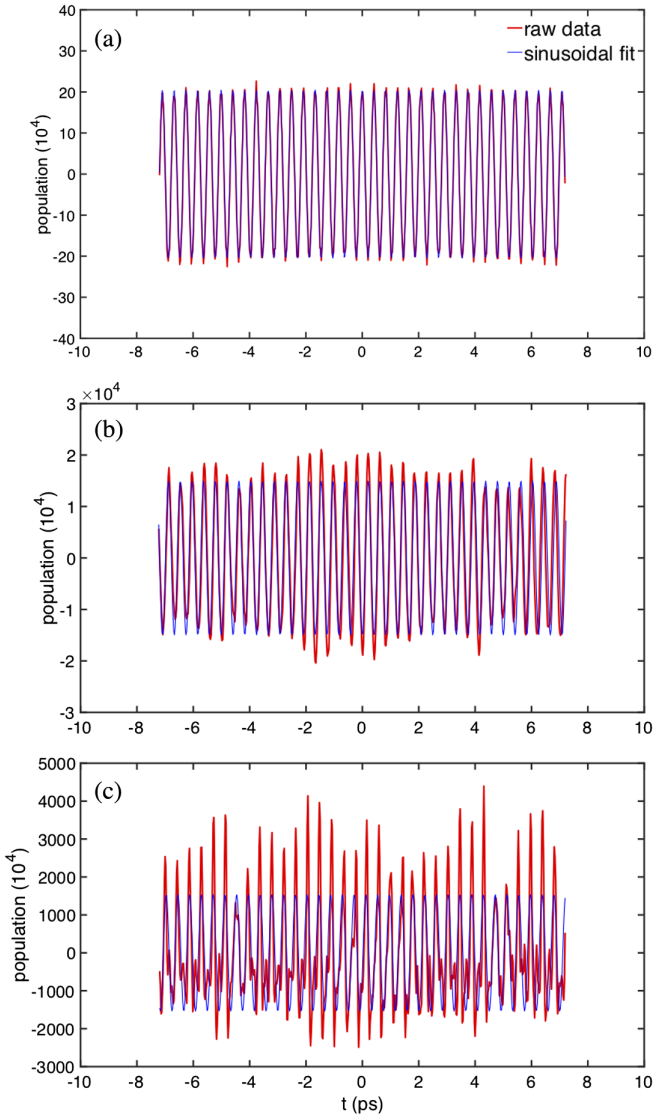

FIG. 10. Particle density distribution along the bunch at (a) $s = 0$ m, the initial location, (b) $s = 93$ m, where the maximum gain locates, and (c) $s = 97$ m, the exit of the beamline. The initial modulation wavelength is assumed 125 μm. Only the steady-state CSR is included in the calculation. The red lines are from the histogram of simulation data (raw data), the blue lines from sinusoidal fit.

(red lines). It can be seen that from Fig. 10(a) and (b) the overlapping between the sinusoidal curve and the raw data is passable. However, the deviation in Fig. 10(c) becomes obvious; the raw data (red curve) appear distorted.

Another way to confirm this numerical observation may resort to Fourier spectrum of the bunch current density, shown in Fig. 11. In Fig. 11(a), where the maximum gain occurs, the spectrum is clearly a single peak at 125 μm or 2.4 THz. However, in Fig. 11(b), the final density modulation is composed of two main components: the fundamental one 125 μm (2.4 THz) and the second-harmonics 62.5 μm (4.8 THz). It is interesting to note that the

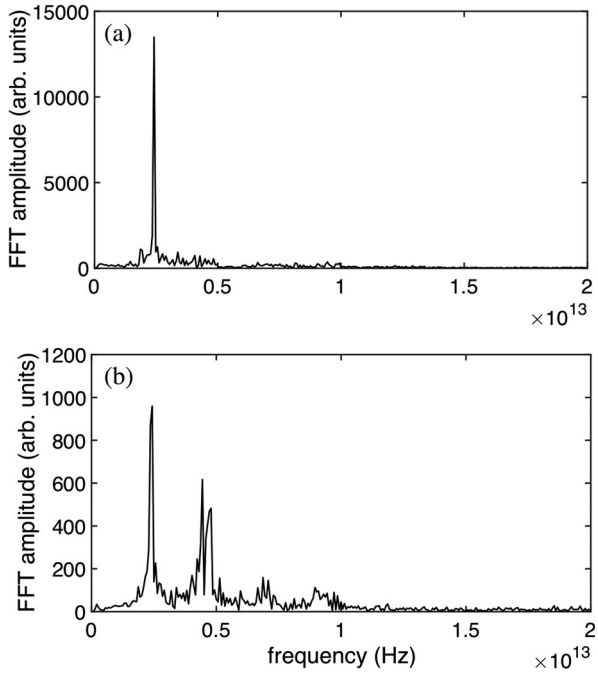

FIG. 11. FFT spectra for the corresponding bunch histograms at $s = 93$ m and 97 m, i.e., Fig. 10(b) and (c), respectively. The initial density modulation is assumed 125 μm, which corresponds to 2.4 THz. It is evident that the higher harmonics emerge in the bottom plot.

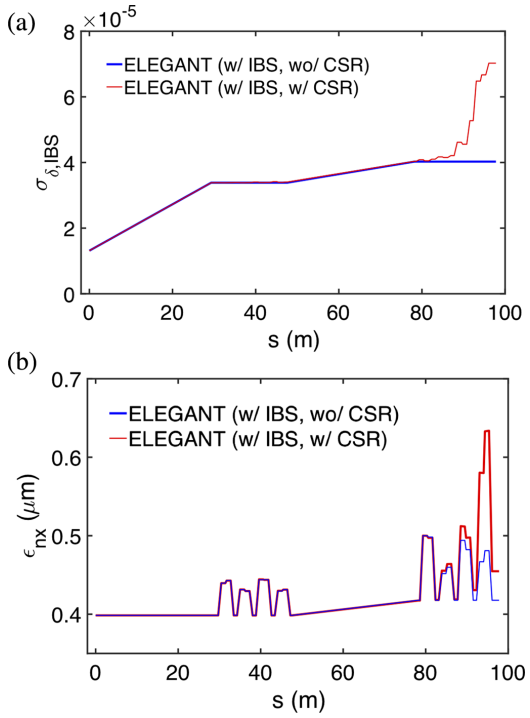

FIG. 12. The evolution of (a) the slice energy spread and (b) the normalized emittance along s. The red lines are for the case with IBS and with (steady-state) CSR; the blue lines without IBS but with (steady-state) CSR. It can be seen that, for (a), about 400% increase for red and ~200% increase for blue. For (b), only 5% increase for blue and 12% increase for red. Here, only the central slices in the bunch are taken for calculation of the slice energy spread and emittance. Those slices close to the bunch head and tail are excluded.

fundamental and the second harmonic components, respectively, occupy about 60% and 40% of the total spectrum, neglecting the remaining higher frequency components. If we *hypothetically* move those leaking to the second harmonics back to the fundamental peak, the FFT amplitude should be recovered by about 66.7%. In other words, the 66.7% reduction of the semianalytical calculation, which is only based on the single-frequency model, may give a consistent prediction to the particle tracking simulation results. The red dashed line in Fig. 9(b) agrees well with ELEGANT results.

It deserves here to discuss one model assumption between the theoretical formulation and the particle tracking simulation. For the former, the growth of the slice transverse emittance and the slice energy spread along the beamline is merely due to IBS; the contribution of collective effects is excluded in the linearized formulation. For the latter, there is no such a restriction: the growth of the slice transverse emittance and the slice energy spread can be contributed by both the IBS and CSR. Using ELEGANT, Fig. 12 shows, in the presence of IBS, the slice energy spread and the transverse emittance with and without CSR along the beamline. The slice parameters are evaluated by taking average over the longitudinal central bunch slices, while excluding the variation due to edge effect from bunch head and tail parts. From Fig. 12 it can be seen that the (fractional) growth of the slice energy spread due to CSR is much larger than that of the slice transverse emittance, and the rapid growth occurs especially at the end of the second arc or near the exit of the beamline. We believe that this rapid growth of the additional slice energy spread will lead to failure of the linear MBI analysis and an unfair comparison with particle tracking simulations.

One may wonder how the IBS may impact MBI when not only steady-state CSR but also other relevant collective effects are present. In addition to computational efficiency, another one major advantage of the semianalytical calculation is that it is straightforward to add relevant impedance models into consideration via $Z_{\parallel}(k_z; s)$ [see, e.g., Eqs. (65) or (A17)]. This will enable us to estimate how the microbunching amplification responds when different collective effects are included. Figure 13 demonstrates the gain spectra when the entrance and exit transient CSR and longitudinal space charge (LSC) are included. The overall gain is higher, while an obvious gain reduction is seen in the high-gain region. The gain reduction due to IBS, as expected, does not play a significant role for a single-turn recirculation. The proposed RIBS ring design, from current perspectives, seems not satisfactory as it is vulnerable to MBI, although the goal of the RIBS ring was to provide the enough slice energy spread to suppress MBI in the

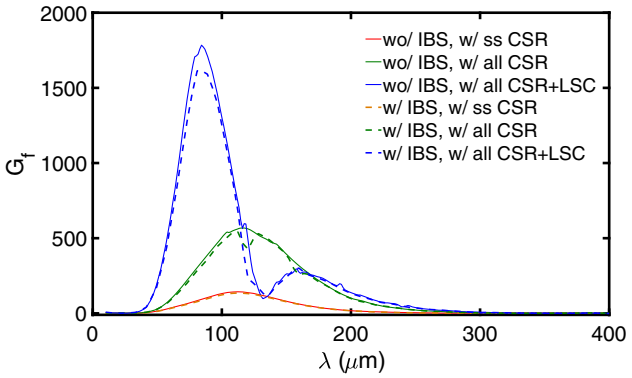

FIG. 13. Gain spectrum at the exit of the recirculating beamline with inclusion of different collective effects and with/without IBS. The all CSR includes steady-state, entrance, and exit transient impedances.

downstream transport line up to the undulator entrance. However the idea (of using RIBS ring to enhance IBS effects) itself may not be completely ruled out, if a better design would be proposed. For example, in Ref. [37], a specialized isochronous arc design with a magnetized beam transport was shown to effectively suppress MBI. If a new RIBS ring were composed of such a specialized arc design, the two straight sections can be used to enhance IBS effects, while the two specialized arcs still preserve the longitudinal beam quality from MBI. Feasibility of this option would require further investigation.

V. SUMMARY AND OUTLOOK

In this paper, we have formulated the effect of the multiple small-angle collision or intrabeam scattering (IBS) on the phase space microbunching dynamics based on the Vlasov-Fokker-Planck (VFP) framework. The corresponding friction and diffusion coefficients are simplified based on the binary-collision model and written as the Landau collision integral form. The fact that a high-brightness relativistic electron beam with $T_{\parallel} \ll T_{\perp}$ further simplifies the integrals and collisional dynamics in the VFP equation. By applying the standard perturbation technique, the VFP equation can be separated to the zeroth-order and the first-order equations. The inflation effect of IBS [Eqs. (1) to (3)] is attributed by the zeroth-order effect, assuming the unperturbed Gaussian phase space distribution, and in the meanwhile contributes to the phase space smearing (or Landau damping). The collective effects [Eqs. (A17)] and the IBS friction and diffusion [Eqs. (A18)] are connected with the first-order dynamics. By defining the phase space density and energy modulations, a set of linear coupled integral equations are obtained and can be numerically solved in an efficient way. We then demonstrate the application of the developed semianalytical formulation to a practical recirculating beamline. The results from the semi-analytical calculation are validated, compared and show good agreement with ELEGANT tracking simulation. Some model assumptions behind the theoretical formulation and particle tracking simulation are discussed. We believe that the developed formulation shall be generally applicable for linear analysis of 6-D phase space dynamics for single-pass high-brightness beams in the presence of both collective and incoherent effects, and hope that it may be applied to further investigate the interplay among the beam collective effects, the incoherent scattering effects.

Here we remark that the present theoretical framework assumes no beam acceleration (or deceleration) nor the bunch compression (or decompression). These are weak points for a direct application of the presented theory to the wider varieties of high-brightness linac-based facilities presently running or planned. The extension can be made by including the bunch compression factor and introducing a set of scaled six-dimensional phase space coordinates. Since the IBS effects, including additional Landau damping through slice energy spread, emittances, and the induced diffusion and friction, depend on the local bunch current (or bunch compression factor) in slightly different ways, the microbunched beam dynamics can be complicated when a beam experiences bunch compression. We have applied the developed semianalytical Vlasov solver to a lattice with bunch compression, where the compressed (larger) beam current would enhance IBS effects, resulting in more pronounced suppression of microbunching instabilities. This work is ongoing; more detailed studies, together with examples involving bunch compression and/or beam acceleration, and investigation on competition between MBI and IBS will be presented in a separate work.

Since the IBS is an accumulation effect, further investigation of the collective phase space microbunching dynamics for the multi-turn recirculation, particularly the dynamical transition from single-pass transport (initial-value problem) to few-passes recirculation and eventually to the storage-ring configuration (eigenvalue problem) may be worth pursuing and is in our plan. In the single-pass theory, as we have formulated in this paper, the every detail of local beam optics (and collective effects of various types) have been considered and the formulation of the phase space dynamics is six-dimensional. On the other hand, most studies of the microwave/microbunching instabilities tend to solve the eigenvalue problems for only two-dimensional longitudinal phase space and the Landau damping depends only on the energy spread and globally averaged optics (and the integrated collective kick) of a storage-ring system (the smooth approximation) [63], where possible local effects might have been overlooked. In storage rings, the energy spread is much larger than that for single-pass or recirculation accelerators and may cause the dominant Landau damping effects, yet this is not true if an accelerator is operated for a few turns of recirculation prior to reaching the equilibrium condition. Studying how the two distinct analyses transit should help bridge the

understanding of the above two scenarios, at least of academic interest.

Finally, we note that recently Di Mitri *et al.* [50] published some interesting experimental evidence of IBS in a linac-driven FEL facility. It deserves here to comment that their simplified analytical estimate includes both beam acceleration and bunch compression. They have studied the impact of the IBS on MBI using FERMI linac facility, and concluded that neglecting IBS effect may result in too conservative facility design or failure to realize accessible potential performance for VUV and soft x-ray FELs [50]. With extension to accommodate the bunch compression/decompression and beam acceleration/deceleration scenarios, we believe that our developed theoretical formulation would be applicable to further investigate the role of both various collective effects and IBS on MBI in the single-pass linac-driven FEL transport line.

ACKNOWLEDGMENTS

One of the authors, C. T., would like to express sincere gratitude to Dr. Simone Di Mitri and Dr. Giovanni Perosa of Elettra-Sincrotrone for many insightful discussions on this work, particularly for S. D. M. for provision of the recirculating beamline lattice file and review of this manuscript. He also thanks Dr. Rui Li and Dr. He Zhang of Jefferson Lab for many helpful discussions and comments of this manuscript, and acknowledges D. P. Chen for help with the preparation of this manuscript. This work is supported by the Fundamental Research Funds for the Central Universities under Project No. 5003131049 and National Natural Science Foundation of China under project No. 11905073.

APPENDIX: DETAILED EXPRESSIONS IN SEC. III D

1. Derivation of the third and fourth terms on rhs of Eq. (44)

By substituting Eq. (53) into the first integral in the third term on rhs of Eq. (44), the term with $D_{z,0}f_1$ is further split into two parts

$$\int D_{z,0}(\tau)f_1(\mathbf{X};\tau)e^{-ik_z(s)z_s(\tau)}\mathrm{d}\mathbf{X} = -\frac{1}{2}\left(\frac{r_e[\mathrm{Log}]}{\gamma^2\epsilon_{\perp,N}^2}\frac{\bar{I}_b}{I_A}\right)\int\left[\frac{\Delta n(z_\tau)}{n_0}+\frac{\delta_\tau\Delta\delta(z_\tau)}{\sigma_{\delta\tau}^2}\right]\mathrm{erf}\left(\frac{\delta_\tau}{\sqrt{2}\sigma_{\delta\tau}}\right)f_0(\mathbf{X};\tau)e^{-ik_z(s)z_s(\tau)}\mathrm{d}\mathbf{X}. \quad \text{(A1)}$$

Note that z_s in the exponent can be expressed in terms of the phase space coordinates at $s=\tau$

$$z_s(\tau) = R_{51}(\tau\to s)x_\tau + R_{52}(\tau\to s)x'_\tau + R_{53}(\tau\to s)y_\tau + R_{54}(\tau\to s)y'_\tau + z_\tau + R_{56}(\tau\to s)\delta_\tau, \quad \text{(A2)}$$

where the relative transport functions from τ to s can be determined using Eq. (48), explicitly expressed as

$$R_{51}(\tau\to s) = [R_{51}(s)-R_{51}(\tau)]R_{22}(\tau) - [R_{52}(s)-R_{52}(\tau)]R_{21}(\tau), \quad \text{(A3a)}$$

$$R_{52}(\tau\to s) = [R_{52}(s)-R_{52}(\tau)]R_{11}(\tau) - [R_{51}(s)-R_{51}(\tau)]R_{12}(\tau), \quad \text{(A3b)}$$

$$R_{53}(\tau\to s) = [R_{53}(s)-R_{53}(\tau)]R_{44}(\tau) - [R_{54}(s)-R_{54}(\tau)]R_{43}(\tau), \quad \text{(A3c)}$$

$$R_{54}(\tau\to s) = [R_{54}(s)-R_{54}(\tau)]R_{33}(\tau) - [R_{53}(s)-R_{53}(\tau)]R_{34}(\tau). \quad \text{(A3d)}$$

To work out the first part of Eq. (A1), we first integrate over δ_τ, then over z_τ, resulting in the density modulation $b(k_z;\tau)$ at $s=\tau$ [see also Eq. (41)]. The remaining integrations over the transverse 4-D phase space coordinate leads to a smearing term. The resultant expression is

$$\begin{aligned}
&\int\frac{\Delta n(z_\tau)}{n_0}\mathrm{erf}\left(\frac{\delta}{\sqrt{2}\sigma_\delta}\right)f_0(\mathbf{X};\tau)e^{-ik_z(s)z_s(\tau)}\mathrm{d}\mathbf{X}\\
&= -i\mathrm{erfi}\left(\frac{1}{2}k_z(s)R_{56}(\tau\to s)\right)e^{-\frac{1}{2}k_z^2(s)R_{56}^2(\tau\to s)\sigma_{\delta\tau}^2}\int\frac{\Delta n(z_\tau)}{n_0}e^{-ik_z(s)z_\tau}\mathrm{d}z_\tau\int f_{0,4D}(\mathbf{X};\tau)e^{-ik_z(s)\sum_{j=1}^4 R_{5j}(\tau\to s)X_{j\tau}}\mathrm{d}\mathbf{X}_{4D}\\
&= -Ni\mathrm{erfi}\left(\frac{1}{2}k_z(s)R_{56}(\tau\to s)\right)\{\mathrm{L.D.};\tau\to s\}b(k_z;\tau),
\end{aligned} \quad \text{(A4)}$$

where $\{\mathrm{L.D.};\tau\to s\}$ is defined as [cf. Eqs. (46) and (50)]

$$\{\text{L.D.};\tau\to s\}=\exp\left\{-\frac{k_z^2(s)}{2}\begin{bmatrix}\epsilon_x^G\beta_{x0}\left(R_{51}(\tau\to s)-\frac{\alpha_{x0}}{\beta_{x0}}R_{52}(\tau\to s)\right)^2+\frac{\epsilon_x^G}{\beta_{x0}}R_{52}^2(\tau\to s)\\ +\epsilon_y^G\beta_{y0}\left(R_{53}(\tau\to s)-\frac{\alpha_{y0}}{\beta_{y0}}R_{54}(\tau\to s)\right)^2+\frac{\epsilon_y^G}{\beta_{y0}}R_{54}^2(\tau\to s)+\sigma_\delta^2R_{56}^2(\tau\to s)\end{bmatrix}\right\}. \tag{A5}$$

In deriving Eq. (A4), the following integration formula has been used [85]

$$\frac{1}{\sqrt{2\pi}\sigma_\delta}\int_{-\infty}^{\infty}\text{erf}\left(\frac{\delta}{\sqrt{2}\sigma_\delta}\right)e^{-\frac{\delta^2}{2\sigma_\delta^2}-iA\delta}\text{d}\delta=-i\text{erfi}\left(\frac{1}{2}A\delta\right)e^{-\frac{1}{2}A^2\sigma_\delta^2} \tag{A6}$$

with $\text{erf}(iz)=i\text{erf}(z)$.

The second part of Eq. (A1) can be evaluated in a similar way, but the energy modulation $p(k_z;\tau)$ at $s=\tau$ would appear [see also Eq. (42)],

$$\begin{aligned}&\int\frac{\delta_\tau\Delta\delta(z_\tau)}{\sigma_{\delta\tau}^2}\text{erf}\left(\frac{\delta_\tau}{\sqrt{2}\sigma_{\delta\tau}}\right)f_0(\mathbf{X};\tau)e^{-ik_z(s)z_s(\tau)}\text{d}\mathbf{X}\\&=\frac{1}{\sqrt{2\pi}\sigma_{\delta\tau}}\int\frac{\delta_\tau}{\sigma_{\delta\tau}^2}\text{erf}\left(\frac{\delta_\tau}{\sqrt{2}\sigma_{\delta\tau}}\right)e^{-\frac{\delta_\tau^2}{2\sigma_{\delta\tau}^2}-ik_z(s)R_{56}(\tau\to s)\delta_\tau}\text{d}\delta_\tau\int\Delta\delta(z_\tau)e^{-ik_z(s)z_\tau}\text{d}z_\tau\int f_{0,4D}(\mathbf{X};\tau)e^{-ik_z(s)\sum_{j=1}^4R_{5j}(\tau\to s)X_{j\tau}}\text{d}\mathbf{X}_{4D}\\&=N2\{\text{L.D.};\tau\to s\}_\perp\sqrt{\frac{2}{\pi}}\frac{1}{\sigma_{\delta\tau}}\left[\sum_{n=0}^{\infty}\frac{(-2)^n(2n-1)!!}{(2n+1)!}\Gamma\left(n+\frac{3}{2}\right){}_1F_1\left(n+\frac{3}{2};\frac{1}{2};-\frac{1}{2}k_z^2(s)R_{56}^2(\tau\to s)\sigma_{\delta\tau}^2\right)\right]p(k_z;\tau),\end{aligned} \tag{A7}$$

where the following integration formula is used [86]

$$\frac{1}{\sqrt{2\pi}\sigma_\delta}\int_{-\infty}^{\infty}\delta\text{erf}\left(\frac{\delta}{\sqrt{2}\sigma_\delta}\right)e^{-\frac{\delta^2}{2\sigma_\delta^2}-iA\delta}\text{d}\delta=\frac{2^{3/2}}{\sqrt{\pi}}\sigma_\delta\left[\sum_{n=0}^{\infty}\frac{(-2)^n(2n-1)!!}{(2n+1)!}\Gamma\left(n+\frac{3}{2}\right){}_1F_1\left(n+\frac{3}{2};\frac{1}{2};-\frac{1}{2}A^2\sigma_\delta^2\right)\right], \tag{A8}$$

where Γ is the gamma function and ${}_1F_1$ is the confluent hypergeometric function [80].

The remaining transverse phase space smearing term is defined as

$$\{\text{L.D.};\tau\to s\}_\perp=\exp\left\{-\frac{k_z^2(s)}{2}\begin{bmatrix}\epsilon_x^G\beta_{x0}\left(R_{51}(\tau\to s)-\frac{\alpha_{x0}}{\beta_{x0}}R_{52}(\tau\to s)\right)^2+\frac{\epsilon_x^G}{\beta_{x0}}R_{52}^2(\tau\to s)\\ +\epsilon_y^G\beta_{y0}\left(R_{53}(\tau\to s)-\frac{\alpha_{y0}}{\beta_{y0}}R_{54}(\tau\to s)\right)^2+\frac{\epsilon_y^G}{\beta_{y0}}R_{54}^2(\tau\to s)\end{bmatrix}\right\}. \tag{A9}$$

For the other term involving f_0 in the third term on the rhs of Eq. (44), it can be analytically integrated in a similar manner

$$\begin{aligned}\int D_{z,1}(\tau)f_0(\mathbf{X};\tau)e^{-ik_z(s)z_s(\tau)}\text{d}\mathbf{X}&=-\frac{1}{2}\left(\frac{r_e[\text{Log}]}{\gamma^2\epsilon_{\perp,N}^2}\frac{\bar{I}_b}{I_A}\right)\int\text{erf}\left(\frac{\delta}{\sqrt{2}\sigma_\delta}\right)\frac{\Delta n(z_\tau)}{n_0}f_0(\mathbf{X};\tau)e^{-ik_z(s)z_s(\tau)}\text{d}\mathbf{X}\\&=N\frac{1}{2}\left(\frac{r_e[\text{Log}]}{\gamma^2\epsilon_{\perp,N}^2}\frac{\bar{I}_b}{I_A}\right)i\text{erfi}\left(\frac{1}{2}k_z(s)R_{56}(\tau\to s)\right)\{\text{L.D.};\tau\to s\}b(k_z;\tau).\end{aligned} \tag{A10}$$

For the fourth term on the rhs of Eq. (44), responsible for the IBS diffusion effect, the detailed derivation is similar and would not be presented here. The resulting expression is

$$\begin{aligned}\int\frac{D_{zz,0}(\tau)}{2}f_1(\mathbf{X};\tau)e^{-ik_z(s)z_s(\tau)}\text{d}\mathbf{X}&=\frac{D_{zz,0}(\tau)}{2}\int\left[\frac{\Delta n(z_\tau)}{n_b}+\frac{\delta_\tau\Delta\delta(z_\tau)}{\sigma_{\delta\tau}^2}\right]f_0(\mathbf{X};\tau)e^{-ik_z(s)z_s(\tau)}\text{d}\mathbf{X}\\&=N\frac{D_{zz,0}(\tau)}{2}\{\text{L.D.};\tau\to s\}[b(k_z;\tau)-ik_z(s)R_{56}(\tau\to s)p(k_z;\tau)]\end{aligned} \tag{A11}$$

for the term with f_1, and the other term involving f_0

$$\int \frac{D_{zz,1}(\tau)}{2} f_0(\mathbf{X};\tau) e^{-ik_z(s)z_s(\tau)} \mathrm{d}\mathbf{X} = N \frac{D_{zz,0}(\tau)}{2} \{\mathrm{L.D.};\tau \to s\} b(k_z;\tau). \tag{A12}$$

This section completes the derivation of the third and fourth terms on the rhs of Eq. (44).

2. The resultant integral equations for $b(k_z;s)$ and $p(k_z;s)$

The complete expression of the integral equation for $b(k_z;s)$ is

$$\begin{aligned}
b(k_z;s) = {} & b_0(k_z;s) + i\int_0^s \frac{\bar{I}_b(\tau)}{\gamma I_A} k_z(s) R_{56}(\tau \to s) Z_\parallel(k_z;\tau) \{\mathrm{L.D.};\tau, s\} b(k_z;\tau) \mathrm{d}\tau \\
& + \int_0^s \left(\frac{r_e[\mathrm{Log}]}{\gamma^2 \epsilon_{\perp,N}^2} \frac{\bar{I}_b}{I_A}\right) k_z(s) R_{56}(\tau \to s) \{\mathrm{L.D.};\tau \to s\} \mathrm{erfi}\left(\frac{1}{2} k_z(s) R_{56}(\tau \to s) \sigma_{\delta\tau}\right) b(k_z;\tau) \mathrm{d}\tau \\
& + i\int_0^s \left(\frac{r_e[\mathrm{Log}]}{\gamma^2 \epsilon_{\perp,N}^2} \frac{\bar{I}_b}{I_A}\right) \{\mathrm{L.D.};\tau \to s\}_\perp \sqrt{\frac{2}{\pi}} \frac{1}{\sigma_{\delta\tau}} \\
& \times \left[\sum_{n=0}^{\infty} \frac{(-2)^n (2n-1)!!}{(2n+1)!} \Gamma\left(n+\frac{3}{2}\right) {}_1F_1\left(n+\frac{3}{2};\frac{1}{2};-\frac{1}{2} k_z^2(s) R_{56}^2(\tau \to s) \sigma_{\delta\tau}^2\right)\right] p(k_z;\tau) \mathrm{d}\tau \\
& - 2\int_0^s \frac{D_{zz,0}(\tau)}{2} k_z^2(s) R_{56}^2(\tau \to s) \{\mathrm{L.D.};\tau \to s\} b(k_z;\tau) \mathrm{d}\tau \\
& + i\int_0^s \frac{D_{zz,0}(\tau)}{2} k_z^3(s) R_{56}^3(\tau \to s) \{\mathrm{L.D.};\tau \to s\} p(k_z;\tau) \mathrm{d}\tau.
\end{aligned} \tag{A13}$$

and that for $p(k_z;s)$ is

$$\begin{aligned}
p(k_z;s) = {} & p_0(k_z;s) - \int_0^s \frac{\bar{I}_b(\tau)}{\gamma I_A} [1 - k_z^2(s) R_{56}^2(\tau \to s) \sigma_{\delta 0}^2] Z_\parallel(k_z;\tau) \{\mathrm{L.D.};\tau, s\} b(k_z;\tau) \mathrm{d}\tau \\
& + i\int_0^s \left(\frac{r_e[\mathrm{Log}]}{\gamma^2 \epsilon_{\perp,N}^2} \frac{\bar{I}_b}{I_A}\right) \{\mathrm{L.D.};\tau \to s\} \mathrm{erfi}\left(\frac{1}{2} k_z(s) R_{56}(\tau \to s)\right) b(k_z;\tau) \mathrm{d}\tau \\
& + 2i\int_0^s \left(\frac{r_e[\mathrm{Log}]}{\gamma^2 \epsilon_{\perp,N}^2} \frac{\bar{I}_b}{I_A}\right) k_z(s) R_{56}(\tau \to s) \{\mathrm{L.D.};\tau \to s\}_\perp \sqrt{\frac{2}{\pi}} \frac{1}{\sigma_{\delta\tau}} \\
& \times \left[\sum_{n=0}^{\infty} \frac{(-2)^n (2n-1)!!}{(2n+1)!} \Gamma\left(n+\frac{3}{2}\right) {}_1F_1\left(n+\frac{3}{2};\frac{1}{2};-\frac{1}{2} k_z^2(s) R_{56}^2(\tau \to s) \sigma_{\delta\tau}^2\right)\right] b(k_z;\tau) \mathrm{d}\tau \\
& - \int_0^s \left(\frac{r_e[\mathrm{Log}]}{\gamma^2 \epsilon_{\perp,N}^2} \frac{\bar{I}_b}{I_A}\right) \{\mathrm{L.D.};\tau \to s\}_\perp \sqrt{\frac{2}{\pi}} \frac{1}{\sigma_{\delta\tau}} \\
& \times \left[\sum_{n=0}^{\infty} \frac{(-2)^n (2n-1)!!}{(2n+1)!} \Gamma\left(n+\frac{3}{2}\right) {}_1F_1\left(n+\frac{3}{2};\frac{1}{2};-\frac{1}{2} k_z^2(s) R_{56}^2(\tau \to s) \sigma_{\delta\tau}^2\right)\right] p(k_z;\tau) \mathrm{d}\tau \\
& + \int_0^s \left(\frac{r_e[\mathrm{Log}]}{\gamma^2 \epsilon_{\perp,N}^2} \frac{\bar{I}_b}{I_A}\right) k_z^2(s) R_{56}^2(\tau \to s) \{\mathrm{L.D.};\tau \to s\}_\perp \frac{2^{3/2}}{\pi} \sigma_{\delta\tau} \\
& \times \left[\sum_{n=0}^{\infty} \frac{(-2)^n (2n-1)!!}{(2n+1)!} \Gamma\left(n+\frac{5}{2}\right) {}_1F_1\left(n+\frac{5}{2};\frac{3}{2};-\frac{1}{2} k_z^2(s) R_{56}^2(\tau \to s) \sigma_{\delta\tau}^2\right)\right] p(k_z;\tau) \mathrm{d}\tau \\
& - 4i\int_0^s \frac{D_{zz,0}(\tau)}{2} k_z(s) R_{56}(\tau \to s) \{\mathrm{L.D.};\tau \to s\} b(k_z;\tau) \mathrm{d}\tau \\
& + 2i\int_0^s \frac{D_{zz,0}(\tau)}{2} k_z^3(s) R_{56}^3(\tau \to s) \sigma_{\delta\tau}^2 \{\mathrm{L.D.};\tau \to s\} b(k_z;\tau) \mathrm{d}\tau \\
& - 3\int_0^s \frac{D_{zz,0}(\tau)}{2} k_z^2(s) R_{56}^2(\tau \to s) \{\mathrm{L.D.};\tau \to s\} p(k_z;\tau) \mathrm{d}\tau \\
& + \int_0^s \frac{D_{zz,0}(\tau)}{2} k_z^4(s) R_{56}^4(\tau \to s) \sigma_{\delta\tau}^2 \{\mathrm{L.D.};\tau \to s\} p(k_z;\tau) \mathrm{d}\tau
\end{aligned} \tag{A14}$$

In deriving Eq. (A14), we have used the following identity [86]

$$\frac{1}{\sqrt{2\pi}\sigma_\delta}\int_{-\infty}^{\infty}\delta^2\mathrm{erf}\left(\frac{\delta}{\sqrt{2}\sigma_\delta}\right)e^{-\frac{\delta^2}{2\sigma_\delta^2}-iA\delta}\mathrm{d}\delta=-iA\frac{2^{5/2}}{\pi}\sigma_\delta^3\left[\sum_{n=0}^{\infty}\frac{(-2)^n(2n-1)!!}{(2n+1)!}\Gamma\left(n+\frac{5}{2}\right){}_1F_1\left(n+\frac{5}{2};\frac{3}{2};-\frac{1}{2}A^2\sigma_\delta^2\right)\right]. \tag{A15}$$

3. Some shorthand notations for the kernel functions

For the IBS-related terms, we define

$$\begin{aligned}D_{z,0}&=-\left(\frac{r_e[\mathrm{Log}]}{\gamma^2\epsilon_{\perp,N}^2}\frac{\bar{I}_b}{I_A}\right)\mathrm{erf}\left(\frac{\delta}{\sqrt{2}\sigma_\delta}\right)\equiv -D_{\mathrm{IBS},z}\mathrm{erf}\left(\frac{\delta}{\sqrt{2}\sigma_\delta}\right),\\ D_{zz,0}&=\frac{\sqrt{\pi}}{2}\left(\frac{r_e[\mathrm{Log}]}{\gamma^2\epsilon_{\perp,N}\sigma_\perp}\frac{\bar{I}_b}{I_A}\right)\equiv\frac{\sqrt{\pi}}{2}D_{\mathrm{IBS},zz},\end{aligned} \tag{A16a}$$

For the kernel functions that involve the collective effect in the integrals, we define

$$K_{Z_\parallel}^{(0)}(\tau,s)=\frac{\bar{I}_b}{\gamma I_A}Z_\parallel(k_z;\tau)\{\mathrm{L.D.};\tau,s\}, \tag{A17a}$$

$$K_{Z_\parallel}^{(1)}(\tau,s)=\frac{\bar{I}_b}{\gamma I_A}k_zR_{56}(\tau\to s)Z_\parallel(k_z;\tau)\{\mathrm{L.D.};\tau,s\}, \tag{A17b}$$

$$K_{Z_\parallel}^{(2)}(\tau,s)=\frac{\bar{I}_b}{\gamma I_A}k_z^2R_{56}^2(\tau\to s)Z_\parallel(k_z;\tau)\{\mathrm{L.D.};\tau,s\}, \tag{A17c}$$

and those involving the IBS

$$K_{\mathrm{IBS},z}^{(n)}(\tau,s)=D_{\mathrm{IBS},z}(\tau)k_z^nR_{56}^n(\tau\to s)\{\mathrm{L.D.};\tau\to s\}\mathrm{erfi}\left(\frac{1}{2}k_z(s)R_{56}(\tau\to s)\sigma_{\delta\tau}\right), \tag{A18a}$$

$$\begin{aligned}K_{\mathrm{IBS},z}^{\perp(0)}(\tau,s)&=D_{\mathrm{IBS},z}(\tau)\{\mathrm{L.D.};\tau\to s\}_\perp\sqrt{\frac{2}{\pi}}\frac{1}{\sigma_{\delta\tau}}\\&\times\left[\sum_{n=0}^{\infty}\frac{(-2)^n(2n-1)!!}{(2n+1)!}\Gamma\left(n+\frac{3}{2}\right){}_1F_1\left(n+\frac{3}{2};\frac{1}{2};-\frac{1}{2}k_z^2(s)R_{56}^2(\tau\to s)\sigma_{\delta\tau}^2\right)\right],\end{aligned} \tag{A18b}$$

$$\begin{aligned}K_{\mathrm{IBS},z}^{\perp(1)}(\tau,s)&=D_{\mathrm{IBS},z}(\tau)k_zR_{56}(\tau\to s)\{\mathrm{L.D.};\tau\to s\}_\perp\sqrt{\frac{2}{\pi}}\frac{1}{\sigma_{\delta\tau}}\\&\times\left[\sum_{n=0}^{\infty}\frac{(-2)^n(2n-1)!!}{(2n+1)!}\Gamma\left(n+\frac{3}{2}\right){}_1F_1\left(n+\frac{3}{2};\frac{1}{2};-\frac{1}{2}k_z^2(s)R_{56}^2(\tau\to s)\sigma_{\delta\tau}^2\right)\right],\end{aligned} \tag{A18c}$$

$$\begin{aligned}K_{\mathrm{IBS},z}^{\perp(2)}(\tau,s)&=D_{\mathrm{IBS},z}(\tau)k_z^2R_{56}^2(\tau\to s)\{\mathrm{L.D.};\tau\to s\}_\perp\frac{2^{3/2}}{\pi}\sigma_{\delta\tau}\\&\times\left[\sum_{n=0}^{\infty}\frac{(-2)^n(2n-1)!!}{(2n+1)!}\Gamma\left(n+\frac{5}{2}\right){}_1F_1\left(n+\frac{5}{2};\frac{3}{2};-\frac{1}{2}k_z^2(s)R_{56}^2(\tau\to s)\sigma_{\delta\tau}^2\right)\right],\end{aligned} \tag{A18d}$$

$$K_{\mathrm{IBS},zz}^{(n)}(\tau,s)=\frac{1}{2}D_{zz,0}(\tau)k_z^nR_{56}^n(\tau\to s)\{\mathrm{L.D.};\tau\to s\}. \tag{A18e}$$

The above shorthand notations are used to simplify Eqs. (A13) and (A14), leading to Eqs. (55) and (56).

[1] M. Dohlus, T. Limberg, and P. Emma, Bunch compression for linac-based FEL's, Electron bunch length compression, ICFA Beam Dyn. Newslett. **38**, 15 (2005).

[2] J. B. Murphy, Coherent synchrotron radiation in storage rings, ICFA Beam Dyn. Newslett. **35**, 20 (2004).

[3] C. Tennant, S. Benson, D. Douglas, R. Li, and C.-Y. Tsai, Studies of CSR and microbunching at the Jefferson Laboratory erls, in *59th ICFA Advanced Beam Dynamics Workshop on Energy Recovery Linacs (ERL'17), Geneva, Switzerland, June 18-23, 2017* (JACOW Publishing, Geneva, Switzerland, 2018), pp. 59–64.

[4] C. Pellegrini, A. Marinelli, and S. Reiche, The physics of x-ray free-electron lasers, Rev. Mod. Phys. **88**, 015006 (2016).

[5] A. Seryi *et al.*, The US electron ion collider accelerator designs, in *North American Particle Accelerator Conference (NAPAC2019), Lansing, MI, USA*, 2019, https://toddsatogata.net/Papers/NAPAC19-MOOHC2.pdf.

[6] J. Beebe-Wang *et al.*, An electron-ion collider study. in *Brookhaven National Laboratory*, 2019, https://wiki.bnl.gov/eic/upload/EIC.Design.Study.pdf.

[7] E. L. Saldin, E. A. Schneidmiller, and M. V. Yurkov, Klystron instability of a relativistic electron beam in a bunch compressor, Nucl. Instrum. Methods Phys. Res., Sect. A **490**, 1 (2002).

[8] S. Heifets, G. Stupakov, and S. Krinsky, Coherent synchrotron radiation instability in a bunch compressor, Phys. Rev. Accel. Beams **5**, 064401 (2002).

[9] Z. Huang and K.-J. Kim, Formulas for coherent synchrotron radiation microbunching in a bunch compressor chicane, Phys. Rev. Accel. Beams **5**, 074401 (2002).

[10] M. Venturini, Microbunching instability in single-pass systems using a direct two-dimensional vlasov solver, Phys. Rev. Accel. Beams **10**, 104401 (2007).

[11] M. Venturini, R. Warnock, and A. Zholents, Vlasov solver for longitudinal dynamics in beam delivery systems for x-ray free electron lasers, Phys. Rev. Accel. Beams **10**, 054403 (2007).

[12] M. Venturini, Models of longitudinal space-charge impedance for microbunching instability, Phys. Rev. Accel. Beams **11**, 034401 (2008).

[13] C.-Y. Tsai, D. Douglas, R. Li, and C. Tennant, Linear microbunching analysis for recirculation machines, Phys. Rev. Accel. Beams **19**, 114401 (2016).

[14] C.-Y. Tsai, Investigation of microbunching instabilities in modern recirculating accelerators, Technical report, Thomas Jefferson National Accelerator Facility, Newport News, VA (United States), 2017.

[15] R. Bonifacio, C. Pellegrini, and L. M. Narducci, Collective instabilities and high-gain regime in a free electron laser, Opt. Commun. **50**, 373 (1984).

[16] K.-J. Kim, Three-dimensional Analysis of Coherent Amplification and Self-amplified Spontaneous Emission in Free-Electron Lasers, Phys. Rev. Lett. **57**, 1871 (1986).

[17] L.-H. Yu, M. Babzien, I. Ben-Zvi, L. F. DiMauro, A. Doyuran, W. Graves, E. Johnson, S. Krinsky, R. Malone, I. Pogorelsky *et al.*, High-gain harmonic-generation free-electron laser, Science **289**, 932 (2000).

[18] E. L. Saldin, E. V. Schneidmiller, and M. V. Yurkov, *The Physics of Free Electron Lasers* (Springer Science & Business Media, New York, 2013).

[19] P. Schmüser, M. Dohlus, J. Rossbach, and C. Behrens, *Free-electron Lasers in the Ultraviolet and X-ray Regime* (Springer Tracts in Modern Physics, New York, 2014), p. 258.

[20] K.-J. Kim, Z. Huang, and R. Lindberg, *Synchrotron Radiation and Free-Electron Lasers* (Cambridge University Press, Cambridge, England, 2017).

[21] L. H. Yu, Generation of intense uv radiation by subharmonically seeded single-pass free-electron lasers. Phys. Rev. A **44**, 5178 (1991).

[22] G. Stupakov, Using the Beam-Echo Effect for Generation of Short-Wavelength Radiation, Phys. Rev. Lett. **102**, 074801 (2009).

[23] D. Xiang and G. Stupakov, Echo-enabled harmonic generation free electron laser, Phys. Rev. Accel. Beams **12**, 030702 (2009).

[24] J. Feldhaus, E. L. Saldin, J. R. Schneider, E. A. Schneidmiller, and M. V. Yurkov, Possible application of x-ray optical elements for reducing the spectral bandwidth of an x-ray sase FEL, Opt. Commun. **140**, 341 (1997).

[25] G. Geloni, V. Kocharyan, and E. Saldin, A novel self-seeding scheme for hard x-ray FELs, J. Mod. Opt. **58**, 1391 (2011).

[26] J. Amann, W. Berg, V. Blank, F.-J. Decker, Y. Ding, P. Emma, Y. Feng, J. Frisch, D. Fritz, J. Hastings *et al.*, Demonstration of self-seeding in a hard-x-ray free-electron laser, Nat. Photonics **6**, 693 (2012).

[27] Z. Zhang, R. Lindberg, W. M. Fawley, Z. Huang, J. Krzywinski, A. Lutman, G. Marcus, and A. Marinelli, Microbunching-instability-induced sidebands in a seeded free-electron laser, Phys. Rev. Accel. Beams **19**, 050701 (2016).

[28] G. Marcus, W. M. Fawley, D. Bohler, Y. Ding, Y. Feng, E. Hemsing, Z. Huang, J. Krzywinski, A. Lutman, and D. Ratner, Experimental observations of seed growth and accompanying pedestal contamination in a self-seeded, soft x-ray free-electron laser, Phys. Rev. Accel. Beams **22**, 080702 (2019).

[29] Z. Zhang, G. Marcus, E. Hemsing, W. M. Fawley, Z. Huang, and A. Lutman, Statistical analysis of a self-seeded x-ray free-electron laser in the presence of the microbunching instability, Phys. Rev. Accel. Beams **23**, 010704 (2020).

[30] N. Kroll, P. Morton, and M. W. Rosenbluth, Free-electron lasers with variable parameter wigglers, IEEE J. Quantum Electron. **17**, 1436 (1981).

[31] S. Isermann and R. Graham, Suppression of the sideband instability in tapered free-electron lasers, Phys. Rev. A **45**, 4050 (1992).

[32] C.-Y. Tsai, J. Wu, C. Yang, M. Yoon, and G. Zhou, Sideband instability analysis based on a one-dimensional high-gain free electron laser model, Phys. Rev. Accel. Beams **20**, 120702 (2017).

[33] E. L. Saldin, E. A. Schneidmiller, and M. V. Yurkov, Longitudinal space charge-driven microbunching instability in the tesla test facility linac, Nucl. Instrum. Methods Phys. Res., Sect. A **528**, 355 (2004).

[34] Z. Huang, M. Borland, P. Emma, J. Wu, C. Limborg, G. Stupakov, and J. Welch, Suppression of microbunching instability in the linac coherent light source, Phys. Rev. Accel. Beams **7**, 074401 (2004).

[35] Z. Huang, A. Brachmann, F.-J. Decker, Y. Ding, D. Dowell, P. Emma, J. Frisch, S. Gilevich, G. Hays, Ph. Hering *et al.*, Measurements of the linac coherent light source laser heater and its impact on the x-ray free-electron laser performance, Phys. Rev. Accel. Beams **13**, 020703 (2010).

[36] D. Ratner, C. Behrens, Y. Ding, Z. Huang, A. Marinelli, T. Maxwell, and F. Zhou, Time-resolved imaging of the microbunching instability and energy spread at the linac coherent light source, Phys. Rev. Accel. Beams **18**, 030704 (2015).

[37] C.-Y. Tsai, Ya. S. Derbenev, D. Douglas, R. Li, and C. Tennant, Vlasov analysis of microbunching instability for magnetized beams, Phys. Rev. Accel. Beams **20**, 054401 (2017).

[38] B. Li and J. Qiang, Mitigation of microbunching instability in x-ray free electron laser linacs, Phys. Rev. Accel. Beams **23**, 014403 (2020).

[39] J. Qiang, S. Lidia, R. D. Ryne, and C. Limborg-Deprey, Three-dimensional quasistatic model for high brightness beam dynamics simulation, Phys. Rev. Accel. Beams **9**, 044204 (2006).

[40] M. Borland, Modeling of the microbunching instability, Phys. Rev. Accel. Beams **11**, 030701 (2008).

[41] G. Bassi, J. A. Ellison, K. Heinemann, and R. Warnock, Microbunching instability in a chicane: Two-dimensional mean field treatment, Phys. Rev. Accel. Beams **12**, 080704 (2009).

[42] C. C. Hall, S. G. Biedron, A. L. Edelen, S. V. Milton, S. Benson, D. Douglas, R. Li, C. D. Tennant, and B. E. Carlsten, Measurement and simulation of the impact of coherent synchrotron radiation on the jefferson laboratory energy recovery linac electron beam, Phys. Rev. Accel. Beams **18**, 030706 (2015).

[43] A. Piwinski, J. D. Bjorken, and S. K. Mtingwa, Wilson prize article: Reflections on our experiences with developing the theory of intrabeam scattering, Phys. Rev. Accel. Beams **21**, 114801 (2018).

[44] M. Venturini, Intrabeam scattering and wake field effects in low emittance electron rings, in *PACS2001. Proceedings of the 2001 Particle Accelerator Conference (Cat. No. 01CH37268)* (IEEE, New York, 2001), vol. 4, pp. 2958–2960.

[45] R. L. Gluckstern and A. V. Fedotov, Coulomb scattering within a spherical beam bunch in a high current linear accelerator, Phys. Rev. Accel. Beams **2**, 054201 (1999).

[46] A. V. Fedotov, Beam halo formation in high-intensity beams, Nucl. Instrum. Methods Phys. Res., Sect. A **557**, 216 (2006).

[47] M. Martini, F. Antoniou, and Y. Papaphilippou, Intrabeam scattering, ICFA Beam Dyn. Newsl. **69**, 38 (2016).

[48] Z. Huang, Intrabeam scattering in an x-ray FEL driver, Technical Report No. LCLS-TN-02-8, Stanford Linear Accelerator Center (SLAC), Menlo Park, CA, 2005.

[49] J. Qiang, Y. Ding, P. Emma, Z. Huang, D. Ratner, T. O. Raubenheimer, M. Venturini, and F. Zhou, Start-to-end simulation of the shot-noise driven microbunching instability experiment at the linac coherent light source, Phys. Rev. Accel. Beams **20**, 054402 (2017).

[50] S. Di Mitri, G. Perosa, A. Brynes, I. Setija, S. Spampinati, P. H. Williams, A. Wolski, E. Allaria, S. Brussaard, L. Giannessi, G. Penco, P. R. Rebernik, and M. Trovò, Experimental evidence of intrabeam scattering in a free-electron laser driver, New J. Phys. **22**, 083053 (2020).

[51] S. Di Mitri, Intrabeam scattering in high brightness electron linacs, Phys. Rev. Accel. Beams **17**, 074401 (2014).

[52] K. Kubo, S. K. Mtingwa, and A. Wolski, Intrabeam scattering formulas for high energy beams, Phys. Rev. Accel. Beams **8**, 081001 (2005).

[53] M. Borland, Elegant: A flexible sdds-compliant code for accelerator simulation, Technical report, Advanced Photon Source LS-287, 2000.

[54] Y. Wang and M. Borland, Pelegant: A parallel accelerator simulation code for electron generation and tracking, AIP Conf. Proc. No. **877**, 241 (2006).

[55] G. Stupakov, Effect of Coulomb collisions on echo-enabled harmonic generation (EEHG), *Proceedings of FEL2011* (Shanghai, China, 2011), MOPB20, pages 49–52, https://accelconf.web.cern.ch/FEL2011/papers/mopb20.pdf.

[56] A. Piwinski, Intra-beam scattering, *9th int. in Conf. on High Energy Accelerators*, 405, 1974, https://cds.cern.ch/record/400720/files/p226.pdf.

[57] J. D. Bjorken and S. K. Mtingwa, Intrabeam scattering. Part. Accel. **13**, 115 (1982).

[58] P. Zenkevich, O. Boine-Frankenheim, and A. Bolshakov, Kinetic effects in multiple intra-beam scattering, AIP Conf. Proc. No. **773**, 425 (2005).

[59] A. Piwinski, Intra-beam scattering in presence of linear coupling, Technical report, Deutsches Elektronen-Synchrotron (DESY), 1990.

[60] S.-Y. Lee, *Accelerator Physics* (World Scientific Publishing, Singapore, 2018).

[61] S. K. Mtingwa and A. V. Tollestrup, Intrabeam scattering formulae for asmptotic beams with unequal horizontal and vertical emittances. Technical report, FERMILAB-PUB-89/224, 1987.

[62] M. Hénon, Vlasov equation? Astron. Astrophys. **114**, 211 (1982).

[63] A. W. Chao, *Physics of Collective Beam Instabilities in High Energy Accelerators* (Wiley, New York, 1993).

[64] A. W. Chao, K. H. Mess *et al.*, *Handbook of Accelerator Physics and Engineering* (World Scientific, Singapore, 2013).

[65] Y. Li, *Studies of the Microwave Instability in the Small Isochronous Ring* (Michigan State University, 2015), https://d.lib.msu.edu/etd/2875.

[66] Y. S. Derbenev, E. L. Saldin, V. D. Shiltsev, and J. Rossbach, Microbunch radiative tail-head interaction, Technical report, TESLA-FEL Report No. 199505, 1995.

[67] J. B. Murphy, R. L. Gluckstern, and S. Krinsky. Longitudinal wake field for an electron moving on a circular orbit, Part. Accel. **57**, 9 (1996).

[68] E. L. Saldin, E. A. Schneidmiller, and M. V. Yurkov, On the coherent radiation of an electron bunch moving in an arc of a circle, Nucl. Instrum. Methods Phys. Res., Sect. A **398**, 373 (1997).

[69] R. Li and C.-Y. Tsai, CSR impedance for non-ultrarelativistic beams, *Proceedings of IPAC2015, Richmond, VA, USA (MOPMN004)* (2015), https://jacowfs.jlab.org/conf/proceedings/IPAC2015/papers/mopmn004.pdf.

[70] R. Li and C.-Y. Tsai, Entrance and exit CSR impedance for non-ultrarelativistic beam, *Proceedings of IPAC2017, Copenhagen, Denmark (WEPIK113)* (2017), https://accelconf.web.cern.ch/ipac2017/papers/wepik113.pdf.

[71] A. Sørensen, Introduction to intrabeam scattering, *Proceedings of the CERN Accelerator School in Århus, Denmark, CERN*, pages 87–10, 1987, https://inspirehep.net/conferences/966130.

[72] V. Lebedev, Single and multiple intrabeam scattering in hadron colliders, AIP Conf. Proc. **773**, 440 (2005).

[73] J. A. Bittencourt, *Fundamentals of Plasma Physics* (Springer Science & Business Media, New York, 2013).

[74] I. S. Gradshteyn and I. M. Ryzhik, *Table of Integrals, Series, and Products* (Academic Press, New York, 2014).

[75] Ya. S. Derbenev and V. D. Shiltsev, Transverse effects of microbunch radiative interaction, Technical report, SLAC-PUB-7181, 1996.

[76] J. Wu, Z. Huang, and P. Emma, Analytical analysis of longitudinal space charge effects for a bunched beam with radial dependence, Phys. Rev. Accel. Beams **11**, 040701 (2008).

[77] C.-Y. Tsai, Concatenated analyses of phase space microbunching in high brightness electron beam transport, Nucl. Instrum. Methods Phys. Res., Sect. A **940**, 462 (2019).

[78] W. H. Press, S. A. Teukolsky, W. T. Vetterling, and B. P. Flannery, *Numerical Recipe in C* (Cambridge University Press, Cambridge, England, 1988).

[79] C.-Y. Tsai, Concatenated analyses of phase space microbunching in high brightness electron beam transport, Nucl. Instrum. Methods Phys. Res., Sect. A **940**, 462 (2019).

[80] J. Mathews and R. L. Walker, *Mathematical Methods of Physics* (WA Benjamin, New York, 1970), vol. 501.

[81] D. R. Douglas, S. V. Benson, A. Hutton, G. A. Krafft, R. Li, G. R. Neil, Y. Roblin, C. D. Tennant, and C.-Y. Tsai, Control of coherent synchrotron radiation and microbunching effects during transport of high brightness electron beams, arXiv:1403.2318.

[82] A. Xiao and M. Borland, Intrabeam scattering effect calculated for a non-gaussian-distributed linac beam, in *Proceedings of the 23rd Particle Accelerator Conference, Vancouver, Canada, 2009* (IEEE, Piscataway, NJ, 2009).

[83] M. Borland, Controlling noise and choosing binning parameters for reliable CSR and LSC simulation in ELEGANT, Technical report, Report No. OAG-TN-2005-027, 2005.

[84] C.-Y. Tsai and R Li, Simulation of coherent synchrotron radiation induced microbunching gain using ELEGANT, Technical report, JLAB-TN-14-016, 2016.

[85] E. W. Ng and M. Geller, A table of integrals of the error functions, J. Res. Nat. Bureau of Standards B **73**, 1 (1969).

[86] Wolfram Research, Inc. Mathematica, Version 12.1. Champaign, IL, 2020.